International Journal of Heat and Mass Transfer 228 (2024) 125620

Contents lists available at ScienceDirect

International Journal of Heat and Mass Transfer

journal homepage: www.elsevier.com/locate/hmt

Numerical investigation of bubble dynamics and flow boiling heat transfer in cylindrical micro-pin-fin heat exchangers

I. El Mellas [a], N. Samkhaniani [b], C. Falsetti [c], A. Stroh [b], M. Icardi [d], M. Magnini [a,*]

[a] Department of Mechanical, Materials and Manufacturing Engineering, University of Nottingham, Nottingham NG7 2RD, United Kingdom
[b] Institute of Fluid Mechanics (ISTM), Karlsruhe Institute of Technologie (KIT), Karlsruhe, D-76131, Germany
[c] Propulsion and Power, Delft University of Technology, Kluyverweg 1, Delft, 2629HS, The Netherlands
[d] School of Mathematical Sciences, University of Nottingham, Nottingham NG7 2RD, United Kingdom

ARTICLE INFO

Keywords:
Pin-fins
Boiling
Micro-evaporator
Two-phase
Bubbles
Volume-of-fluid

ABSTRACT

Micro-pin-fin evaporators are a promising alternative to multi-microchannel heat sinks for two-phase cooling of high power-density devices. Within pin-fin evaporators, the refrigerant flows through arrays of obstacles in cross-flow and is not restricted by the walls of a channel. The dynamics of bubbles generated upon flow boiling and the associated heat transfer mechanisms are expected to be substantially different from those pertinent to microchannels; however, the fundamental aspects of two-phase flows evolving through micro-pin-fin arrays are still little understood. This article presents a systematic analysis of flow boiling within a micro-pin-fin evaporator, encompassing bubble, thin-film dynamics and heat transfer. The flow is studied by means of numerical simulations, performed using a customised boiling solver in OpenFOAM v2106, which adopts the built-in geometric Volume of Fluid method to capture the liquid–vapour interface dynamics. The numerical model of the evaporator includes in-line arrays of pin-fins of diameter of 50 μm and height of 100 μm, streamwise pitch of 91.7 μm and cross-stream pitch of 150 μm. The fluid utilised is refrigerant R236fa at a saturation temperature of 30 °C. The range of operating conditions simulated includes values of mass flux G = 500–2000 kg/(m^{2}s), heat flux q = 200 kW/m^2, and inlet subcooling ΔT_{sub} = 0–5 K. This study shows that bubbles nucleated in a pin-fin evaporator tend to travel along the channels formed in between the pin-fin lines. Bubbles grow due to liquid evaporation and elongate in the direction of the flow, leaving thin liquid films that partially cover the pin-fins surface. The main contributions to heat transfer arise from the evaporation of this thin liquid film and from a cross-stream convective motion induced by the bubbles in the gap between the cylinders, which displace the hot fluid otherwise stagnant in the cylinders wakes. When the mass flow rate is increased, bubbles depart earlier from the nucleation sites and grow more slowly, which results in a reduction of the two-phase heat transfer. Higher inlet subcooling yields lower two-phase heat transfer coefficients because condensation becomes important when bubbles depart from the hot pin-fin surfaces and reach highly subcooled regions, thus reducing the two-phase heat transfer.

1. Introduction

With the increasing demand for data computing and processing and the miniaturisation of electronic devices, the heat that needs to be dissipated per unit surface area from electronic components is dramatically increasing. Devices such as computer chips, high-power electronics found in aerospace systems, nuclear reactors, batteries and fuel cells will require dissipation of heat fluxes on the order of 1 MW/m^2 and above [1]. Flow boiling in multi-microchannel evaporators has emerged as an efficient thermal management solution for these high power-density applications, thanks to the advantages of two-phase flow characteristics such as uniform temperature field, high heat transfer coefficients owing to the removal of the latent heat, and the possibility of adopting dielectric refrigerants in direct contact with the surface to be refrigerated [2]. For these reasons, flow boiling in microchannels has been studied extensively in recent years, and a number of review papers have been dedicated to the underlying fluid dynamics and heat transfer aspects [1,3–5]. Pin-fin micro-evaporators represent an alternative geometry to microchannels. Within these evaporators, the fluid is not arranged within straight, isolated channels but it flows across arrays of cylindrical obstacles in cross-flow [6]. The pin-fins create disturbance on the flow field and promote the flow mixing, thus potentially enhancing the heat transfer coefficient with respect

* Corresponding author.
E-mail address: mirco.magnini@nottingham.ac.uk (M. Magnini).

https://doi.org/10.1016/j.ijheatmasstransfer.2024.125620
Received 23 October 2023; Received in revised form 14 March 2024; Accepted 23 April 2024
Available online 30 April 2024

to traditional straight channels [6]. Comprehensive reviews covering heat transfer enhancement using pin-fin microevaporators, including their fabrication, geometrical arrangements, single- and two-phase heat transfer and pressure drop, have been published by Mohammadi and Kosar [7] and Deng et al. [8]. The research on pin-fin heat sinks has mainly focused on reducing the pressure drop in the evaporator while increasing the heat transfer performance. However, the investigation of thermal phenomena and fluid dynamics of two-phase flows within micro-pin-fin evaporators has received far less attention than the conventional multi-microchannel evaporators. From the available literature, it can be found that experiments in micro-pin-fin evaporators have been carried out for various pin-fin shapes such as circular, triangular, square, diamond-shaped, and piranha fins [9–13]. These studies have shown that triangular and rhomboidal pin-fins tend to outperform other shapes in terms of heat transfer performance. However, circular pin-fins may result in a more homogeneous flow distribution, which can benefit the heat transfer performance. Additionally, the density of pin-fins has been identified as a significant factor affecting two-phase pressure drop. Kosar et al. [14,15] investigated the thermal and hydraulic performances of circular and hydrofoil-shaped pin-fins, with the diameter of the circular obstacles, $d_h = 99.5\,\mu m$, matching the thickness of the hydrofoils, using R123 as the working fluid. Heat transfer coefficients were reported to increase with the applied heat flux at lower heat flux levels, which was associated with a nucleate boiling behaviour, whereas they decreased when increasing heat flux at high heat flux values, which was associated with a convective boiling behaviour. Krishnamurthy et al. [16] performed experiments with staggered arrays of circular micro-pin-fins of $d_h = 100\,\mu m$ using water as working fluid. They found that the two-phase heat transfer coefficient was moderately dependent on the mass flux and independent of the heat flux, suggesting that convective boiling was the dominant heat transfer mechanism. Law et al. [17] experimentally compared the pressure drop and heat transfer of a conventional multi-microchannel evaporator with an evaporator with oblique-finned microchannels, i.e. where the straight parallel channels were communicating via oblique passages so that the overall configuration could be interpreted as that of arrays of rhomboidal pin-fins. They reported that the heat transfer coefficient, critical heat flux and pressure drop were significantly higher for the oblique-finned channels, which was attributed to a disruption of the thin liquid film developing over the channel walls. Falsetti et al. [18–20] characterised the heat transfer performance of a micro-evaporator with arrays of in-line cylindrical pin-fins of diameter of $50\,\mu m$, for different refrigerant fluids. Vapour bubbles were observed to nucleate over the surface of the pin-fins and grow along the gaps in between the pin-fins arrays [20]. Contrasting heat transfer coefficient trends were observed as a function of heat and mass flux depending on the fluid. For R236fa, the heat transfer coefficient increased with increasing heat flux, and decreased with increasing mass flux for $q = 20\,W/cm^2$, whereas it was weakly dependent on the mass flux for $q = 44\,W/cm^2$ [18]. When employing fluid R1234ze(E) [19], the heat transfer coefficient was weakly dependent on heat flux for mass fluxes up to $G = 1500\,kg/(m^2s)$, but increased with heat flux for $G = 1700\,kg/(m^2s)$; moreover, the heat transfer performances were observed to improve when increasing the mass flux across the entire range of heat fluxes tested ($q = 28 - 44\,W/cm^2$). For R134a [20], the heat transfer coefficient was enhanced when increasing the mass flux but was reduced when increasing the heat flux. However, when plotting the heat transfer coefficient as a function of the streamwise coordinate along the evaporator rather than as a function of the vapour quality, the heat flux was observed to have only a minor effect. Chang et al. [21] investigated the effect of the inlet subcooling on flow boiling in square pin-fin evaporators and reported that increasing the level of subcooling had the effect of delaying boiling incipience to higher heat fluxes, reducing the bubble diameter and departure frequency and thereby slightly reducing the subcooled flow boiling heat transfer coefficient.

While numerical simulations have been extensively used to study flow boiling in straight microchannels [22–24], their application to the analysis of two-phase flows across pin-fin arrays is still infrequent. To the authors' knowledge, the only study relevant to boiling in pin-fin evaporators was performed by Lorenzini and Joshi [25] who analysed the development of flow patterns and heat transfer performances for geometries with variable pin densities. El Mellas et al. [26] performed fundamental two-phase simulations to study the dynamics of an elongated bubble translating between two arrays of in-line cylindrical pin-fins. Although the study was limited to adiabatic conditions, it revealed that a thin liquid film remained trapped between the bubble and the walls of the pin-fins, and the thickness of this film was smaller than that reported for bubbles translating in straight channels at the same conditions.

In summary, the literature on experimental studies reviewed above emphasises that, for micro-pin-fin evaporators, there is substantial disagreement on the effect that key operating conditions such as vapour quality, heat flux and mass flux have on flow boiling heat transfer. Although flow visualisation techniques have been adopted, these are still limited by the small spatio-temporal scales of the flow. Thus, the essential hydrodynamics details of two-phase flows remain elusive.

In this work, the fundamental heat and mass transfer aspects of flow boiling in a micro-pin-fin evaporator are investigated by means of detailed interface-resolving numerical simulations for the first time. Simulations are performed using a geometrical Volume Of Fluid (VOF) method in OpenFOAM v2106, using a self-developed solver that incorporates specific libraries to improve surface tension and calculate the liquid–vapour mass transfer due to evaporation [24]. The evaporator geometry and operating conditions are taken from the experimental work of Falsetti et al. [18]. The evaporator is composed of in-line arrays of cylindrical pin-fins with diameter, height, and streamwise pitch of $50\,\mu m$, $100\,\mu m$ and $91.7\,\mu m$, respectively. The cross-stream distance between the arrays is $150\,\mu m$. The fluid used is R236fa at the saturation temperature of $T_{sat} = 30\,°C$ ($p_{sat} = 320\,kPa$), for mass fluxes in the range $G = 500 - 2000\,kg/(m^2s)$, heat flux fixed to $q = 200\,kW/m^2$, and inlet subcooling ranging from 0 K to 5 K. This work investigates the two-phase flow dynamics during the growth of bubbles across the pin-fin arrays, as well as the effect of the mass flow rate, the nucleation site location and inlet subcooling, on the heat transfer performance.

This paper is organised as follows: the numerical framework is introduced in Section 2; geometry and boundary conditions are described in Section 3 and the results of the grid independence analysis in Section 4. Section 5 outlines the results of the simulations, and the conclusions of this work are summarised in the final Section 6.

2. Numerical framework

Direct numerical simulations are performed using the open-source library OpenFOAM, version v2106. The numerical model adopts the Volume Of Fluid (VOF) method to track the interface between liquid and vapour [27], using the built-in geometric VOF library based on the work of Roenby et al. [28] and Scheufler and Roenby [29]. Furthermore, the solver we utilise in our simulations includes additional strategies to reduce the spurious currents generated by inaccuracies in the surface tension calculation and implements a phase-change model based on the Hertz–Knudsen–Schrage relationship [30]. The solver was described in detail by Municchi et al. [24], where a number of validation tests were performed. The continuity, momentum, and energy equations are formulated as follows:

$$\nabla \cdot \boldsymbol{u} = \frac{\dot{\rho}}{\rho} \tag{1}$$

$$\frac{\partial(\rho \boldsymbol{u})}{\partial t} + \nabla \cdot (\rho \boldsymbol{u}\boldsymbol{u}) = -\nabla p + \nabla \cdot \mu \left[(\nabla \boldsymbol{u}) + (\nabla \boldsymbol{u})^T \right] + \boldsymbol{F_\sigma} \tag{2}$$

$$\frac{\partial(\rho c_p T)}{\partial t} + \nabla \cdot (\rho c_p \boldsymbol{u}) = \nabla \cdot (\lambda \nabla T) + \dot{h} \tag{3}$$

where $\boldsymbol{u}$ is the velocity, $\dot{\rho}$ the mass flux due to phase-change, ρ the mixture fluid density, t the time, p the pressure, μ the dynamic viscosity, $\boldsymbol{F_\sigma}$ the surface tension force vector, T the temperature, c_p the constant pressure specific heat, λ the thermal conductivity, and $\dot{h}$ is the enthalpy source due to phase-change. Within the range of conditions simulated, the Bond number of the flow is very small, which supports the approximation of negligible gravitational forces. As customary for the VOF method, a volume fraction field α is defined to identify the different phases throughout the flow domain. In each computational cell of the domain, α identifies the fraction of the computational cell volume occupied by the primary phase, which coincides with liquid in the present study. Therefore, the volume fraction takes values of 1 in the liquid, 0 in the gas, and $0 < \alpha < 1$ in the interfacial cells, where the liquid–gas interface can be found. Accordingly, an additional transport equation for the volume fraction is solved:

$$\frac{\partial \alpha}{\partial t} + \nabla \cdot (\alpha \boldsymbol{u}) = \frac{\dot{\rho}}{\rho}\alpha \tag{4}$$

Using the volume fraction field, the properties of the mixture fluid can be computed as an average over the two phases, e.g. $\rho = \alpha\rho_l + (1-\alpha)\rho_g$, with the subscripts g and l denoting gas-specific and liquid-specific properties, respectively. All the fluid-specific properties (e.g. ρ_g, ρ_l, μ_g, μ_l, etc.) are considered constant in this work.

The surface tension force, $\boldsymbol{F_\sigma}$ in Eq. (2), is formulated according to the Continuum Surface Force method [31] and computed as:

$$\boldsymbol{F_\sigma} = \frac{2\rho}{\rho_l + \rho_g}\sigma\kappa|\nabla\alpha| \tag{5}$$

where σ is the surface tension coefficient (considered constant) and κ is the local interface curvature. The accuracy in the approximation of the surface tension force is crucial in these simulations where the capillary number is small and the flow is driven by capillary forces. To enhance the calculation of surface tension compared to the native version of OpenFOAM, the density correction term $2\rho/(\rho_l + \rho_g)$ is introduced to redistribute the surface force towards the heavier fluid region, and the interface curvature is calculated based on the gradients of a smoothed volume fraction field as explained and demonstrated by Municchi et al. [24].

The mass and enthalpy source terms due to evaporation, $\dot{\rho}$ and $\dot{h}$ in Eqs. (4), (1) and (3), are calculated according to the model of Hardt and Wondra [32]. The evaporation mass flux at the interface, $\dot{m}$, is calculated as a function of the local interface superheat according to the Hertz–Knudsen–Schrage relationship [30], and adopting the linearisation proposed by Tanasawa [33] for low values of superheat:

$$\dot{m} = \frac{2\gamma}{2-\gamma}\left(\frac{M}{2\pi R_g}\right)^{1/2}\frac{\rho_g h_{lv}(T_{lv} - T_{sat})}{T_{sat}^{3/2}} \tag{6}$$

where γ is the evaporation coefficient, h_{lv} is the vaporisation latent heat, R_g is the universal gas constant, M is the molecular weight of the fluid, T_{lv} is the temperature at the interface, and T_{sat} the saturation temperature of the fluid. The evaporation coefficient is set to $\gamma = 1$ in all the simulations performed in this work in agreement with preliminary test benchmarks [24]. A first volumetric mass source $\dot{\rho}_0$ is evaluated by calculating the evaporating mass flux based on the temperature on the liquid side of the interface:

$$\dot{\rho}_0 = N\alpha|\nabla\alpha|\dot{m} \tag{7}$$

where N is a normalisation factor to ensure that the global evaporation rate is preserved [32]. A smoothed evaporation mass source $\dot{\rho}_1$ is then evaluated by solving a steady diffusion equation to improve numerical stability [32,34]. From $\dot{\rho}_1$, the final volumetric source $\dot{\rho}$ is obtained by redistributing the smoother evaporation rate across the interface on the vapour and liquid sides as follows:

$$\dot{\rho} = \begin{cases} N_v(1-\alpha)\dot{\rho}_1, & \text{if } \alpha < \alpha_{cut} \\ -N_l\alpha\dot{\rho}_1, & \text{if } \alpha > 1-\alpha_{cut} \\ 0, & \text{if } \alpha_{cut} < \alpha < 1-\alpha_{cut} \end{cases} \tag{8}$$

where N_l, N_v are normalisation factors that guarantee that the mass of liquid evaporated and vapour created are conserved by the redistribution step. The threshold parameter α_{cut} is set to 10^{-3}, ensuring that the evaporation source term is non-zero only on vapour- or liquid-full cells. The enthalpy source $\dot{h}$ accounts for the latent heat of evaporation and is calculated from the initial volumetric source term as $\dot{h} = -\dot{\rho}_0 h_{lv}$.

The governing equations are solved using a custom solver in OpenFOAM v2106. The geometric VOF solver isoAdvector is used to solve the volume fraction equation [28,29]. All other equations are integrated in time with a first-order implicit method. The divergence operators are discretised using second-order TVD (Total Variation Diminishing) schemes [35], whereas Laplacian operators are discretised with central finite differences. The PISO (Pressure Implicit Splitting of Operators) algorithm [36] is utilised to iteratively update pressures and velocities (*momentumPredictor yes*; *nCorrectors 3*) within each time-step. The residuals thresholds for the iterative solution of the flow equations are set to 10^{-7} for the velocity, 10^{-8} for the pressure, 10^{-8} for the volume fraction, and 10^{-10} for the temperature and the evaporation source term smoothing equation. The simulation time step is adaptively chosen to have a maximum local Courant number below 0.2.

3. Simulations setup

3.1. Geometry

The geometry and conditions for the simulations are taken from the work of Falsetti et al. [18], where the thermohydraulic performances of a micro-pin-fin evaporator were experimentally characterised, using the refrigerant R236fa as working fluid with the outlet saturation temperature maintained constant at $T_{sat} = 30.5 \pm 0.5\,°C$. The working conditions analysed by the experiments involved a range of mass fluxes of $G = 500 - 2500\,\mathrm{kg/(m^2 s)}$ and heat fluxes of $q = 20 - 48\,\mathrm{W/cm^2}$. The micro-evaporator was traversed by 66 in-line rows of circular micro-pin-fins, covering a total heated area of $1\,\mathrm{cm^2}$. Two versions of the micro-evaporator were tested, one with and one without inlet restrictions. The inlet restrictions consisted of an additional row of pin-fins with a larger diameter placed before the heated area to suppress flow instabilities, such as vapour backflow [18]. In the present numerical work, the geometrical configuration of the micro-pin-fin evaporator is simulated by considering up to three arrays of pin-fins and the adjacent channels, depending on the study being performed; a schematic of the flow configuration and notation in this work is provided in Fig. 1. The flow domain is represented with a three-dimensional geometry. A Cartesian coordinate system is adopted to describe the flow, where x indicates the streamwise coordinate, y is the width-wise cross-stream coordinate, and z is the height-wise cross-stream coordinate. The coordinate system is centred between two pin-fin arrays, and $z = 0$ identifies the bottom surface of the evaporator, where heat is applied.

Fig. 1(b) shows an illustration of the flow domain used for the two-phase simulations described in Sections 5.2, 5.3 and 5.4, where two arrays of pin-fins are included in the geometry. The circular micro-pin-fins have a radius and height of respectively $R = 25\,\mu\mathrm{m}$ and $H = 100\,\mu\mathrm{m}$; the pitch between the cylinders in the streamwise and cross-stream directions are respectively $d_x = 91.7\,\mu\mathrm{m}$ and $d_y = 150\,\mu\mathrm{m}$. The cross-stream gap between the cylinders identifies a square channel of width $W_{ch} = d_y - 2R = 100\,\mu\mathrm{m}$. The hydraulic diameter of the channels d_h is identified as the hydraulic diameter of this square cross-section, i.e. $d_h = 100\,\mu\mathrm{m}$ [18]. Larger cylinders, of radius of $50\,\mu\mathrm{m}$, are positioned upstream the channel to serve as inlet restrictions [18]. In the example of Fig. 1(b), the domain width is $W = 300\,\mu\mathrm{m}$, which incorporates two arrays of cylinders and the adjacent channels. The domain length will be varied in this work in the range $L = 2-10\,\mathrm{mm}$, depending on the flow conditions investigated. The working fluid tested is the refrigerant R236fa, which will be studied for a saturation temperature of 30 °C; the thermophysical properties of the fluid at the conditions of interest are listed in Table 1.

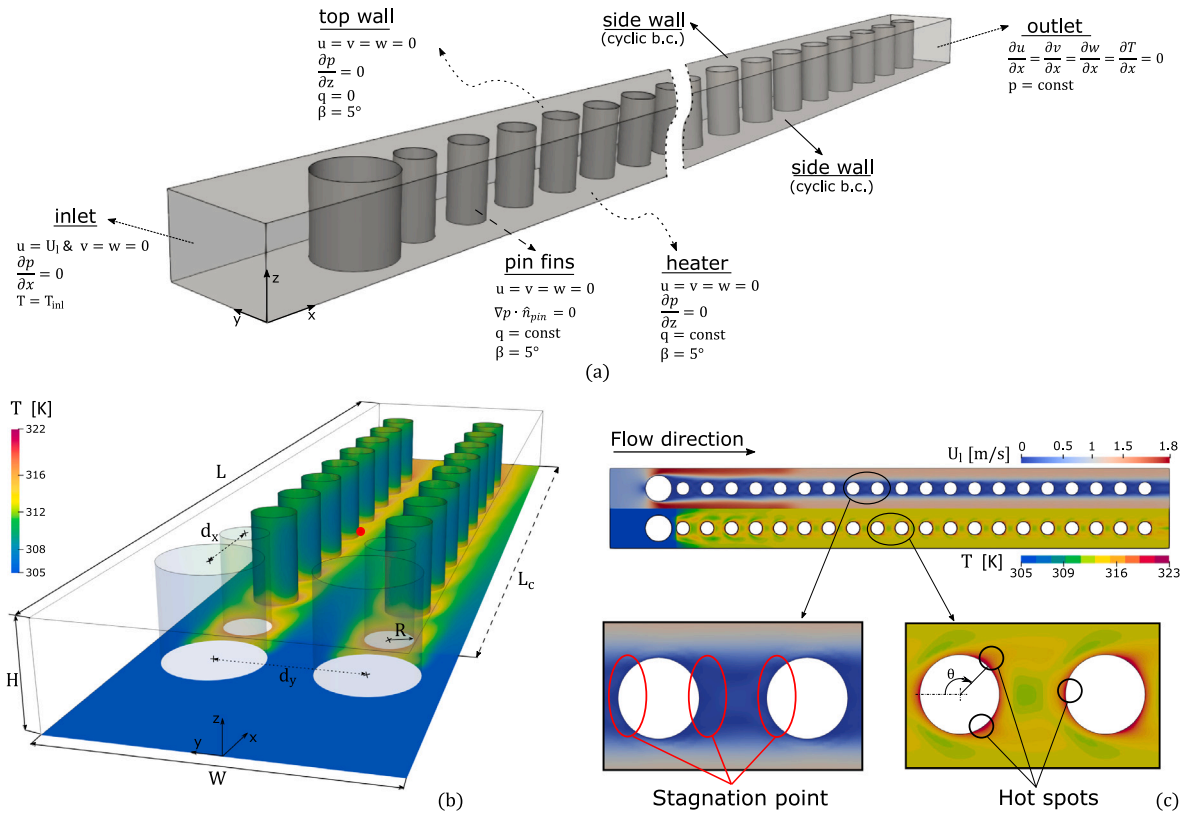

Fig. 1. (a) Schematic of the simulation geometry and boundary conditions; for convenience, only one row of pins is shown. (b) Illustration of the flow domain and notation used in this work. The temperature contours of the heated surfaces are shown, extracted at the start of a two-phase simulation. The domain width, length, and height are indicated with W, L and H, respectively. For visualisation, a short domain of length $L = 50R$ is displayed. R denotes the radius of the cylindrical pins. The streamwise (along x) and cross-stream (along y) distances between the cylinders' centres are indicated as d_x and d_y. The length of the heated area is denoted with L_c. The flow is in the direction of positive x. The red dot identifies a plausible nucleation site for the two-phase simulation. (c, top half) Velocity contours on a horizontal plane halfway through the domain height ($z = H/2$) and (c, bottom half) temperature contours of the heater ($z = 0$) at the start of the two-phase simulation. Simulation conditions: $G = 1000\,\mathrm{kg/(m^2s)}$, $q = 200\,\mathrm{kW/m^2}$, $T_{sat} = 30\,^\circ\mathrm{C}$ and no inlet subcooling. (For interpretation of the references to colour in this figure legend, the reader is referred to the web version of this article.)

Table 1
Thermophysical properties of the refrigerant R236fa at $T_{sat} = 30\,^\circ\mathrm{C}$ ($p_{sat} = 320\,\mathrm{kPa}$).

Phase	ρ [kg/m^3]	λ [W/(m K)]	μ [kg/(m s)]	σ [N/m]	h_{lv} [kJ/kg]
liquid	1342.4	0.0714	2.675×10^{-4}	0.008933	142.42
vapour	21.57	0.01436	1.119×10^{-5}		

3.2. Boundary conditions

The boundary conditions for the geometry are illustrated in Fig. 1(a). At the inlet ($x = 0, y, z$), a liquid-only flow of uniform velocity is imposed (U_l), together with a zero-gradient condition for the pressure; the fluid velocity is calculated from the target value of the mass flux as $U_l = GW_{ch}/[\rho_l(W_{ch} + 2R)]$. The temperature of the working fluid at the inlet is set to a value of $T_{inl} = T_{sat} - \Delta T_{sub}$, with ΔT_{sub} being the target value of the inlet subcooling. At the fluid outlet ($x = L, y, z$), a zero-gradient condition is imposed for the velocity and the temperature, with a reference pressure value. Periodic boundary conditions are adopted at the sides of the domain ($x, |y| = W/2, z$) to model the presence of adjacent channels. In the experiment, the heat load was applied through the evaporator base and transferred to the operating fluid through the pin-fins and bottom channel surface. Since the numerical model does not account for conjugate heat transfer, a constant heat flux q is applied to the cylinders' surface and to the bottom boundary of the evaporator ($x, y, z = 0$). The heat load is not applied to the entire domain length but only along a length L_c measured starting from the centre of the larger cylinders at the inlet; this emulates the experimental setup, where heat was applied via Aluminium heaters covering only the channel area of the evaporator and not the inlet and outlet manifolds. In the experiment, the top of the evaporator was covered with a glass lid to allow optical access. This is reproduced in the numerical model by setting an adiabatic condition to the top of the domain ($x, y, z = H$). On the channel and pin-fin walls, a no-slip condition is applied. The contact angle formed by the liquid–vapour interface and the solid walls is set to a static value of $\beta = 5°$ (hydrophilic wall). In the experiment, the contact angle of R236fa on silicon was not measured. Since R236fa is an almost perfectly wetting fluid, the contact angle was arbitrarily set to a small value.

The working conditions investigated in the present numerical study involve a range of mass fluxes of $G = 500 - 2000\,\mathrm{kg/(m^2s)}$, a range of inlet subcooling values of $\Delta T_{sub} = 0 - 5\,\mathrm{K}$, while the heat flux is fixed to $q = 20\,\mathrm{W/cm^2}$.

3.3. Initial conditions

Two-phase flow simulations require seeding an initial bubble and suitable initial velocity and temperature fields. The latter can be obtained from a preliminary single-phase simulation run under the same conditions, which emulates the initial stage of the experiment where heat is applied to the evaporator and the fluid temperature increases over time until nucleation begins. Due to the high heat flux applied in the flow boiling experiments, this preliminary single-phase simulation cannot be run until steady-state, because the wall temperature would increase to several tens of degrees above saturation, which is unrealistic. Therefore, the single-phase simulation was run in time until the wall temperature reached a prescribed target value at a specified nucleation point, both identified as explained below.

The velocity and temperature contours displayed in Fig. 1(b) and (c) show an example of initial conditions for a two-phase simulation taken from a single-phase simulation that was not run until steady-state. The exact locations of the nucleation points of the bubbles are generally not known a priori. However, potential sites can be identified where micro-cavities are present in the walls due to the microfabrication process [37]. One plausible location is at the edge where the pin-fin surface meets the base surface of the channel [17,18], because temperatures are higher due to the presence of the hydrodynamic boundary layers and the photolithography manufacturing procedure may leave some surface imperfections at the connecting point between the flat base surface and the cylinder, which will act as nucleation spots. This point is highlighted in Fig. 1(b) with a red dot at the base of the fifth pin-fin on the left-hand side array. The fifth cylinder was adopted as the nucleation point in the simulations with no inlet subcooling, whose results are discussed in Sections 5.1.2, 5.2, 5.3 and 5.4. The choice of the fifth cylinder was arbitrary and made as a compromise between placing the nucleation point too close to the inlet restrictions and the computational cost of increasing the length of the domain. The circumferential location of the nucleation spot around the selected pin-fin was chosen upon inspection of the single-phase temperature fields; see, for example, Fig. 1(c). The hottest zone of each pin-fin was identified as a spot located at about 135° from the stagnation point at the cylinder upstream, which coincides with the point where the hydrodynamic boundary layer separates from the cylinder surface. Therefore, this circumferential location was identified as the most suitable for nucleation; interestingly, this location around the cylinder corresponds qualitatively to the point where Falsetti et al. [20] observed streams of bubbles being generated by the nucleation process.

The nucleation temperature is a result of the topography of the surface over which boiling occurs and of the hydraulic and thermal boundary layers developing over the wall, which impact the near-wall temperature profile. The nucleation temperature was not measured in the experiment, and thus, an estimation must be extracted from the available experimental data. Falsetti et al. [18] reported curves of the heat transfer coefficient as a function of the vapour quality for a few selected values of the mass flux G and heat flux q. For a given G and q pair, the heat transfer coefficient corresponding to a zero vapour quality can be assumed as the heat transfer coefficient at the boiling onset. From this value of the heat transfer coefficient, a wall temperature at the boiling onset can be back-calculated from $h = q/(T_w - T_{sat})$, with h being the heat transfer coefficient from the experiment and T_w the unknown nucleation temperature.

In summary, the general procedure to obtain suitable initial velocity and temperature conditions for a two-phase simulation is as follows: (i) for the selected set of working conditions (G and q) to be investigated, a nucleation temperature is estimated from the knowledge of the heat transfer coefficient from the experimental data in Falsetti et al. [18]; (ii) a nucleation location is arbitrarily defined as a point at the edge between the fifth pin-fin and the base surface, forming an angle of 135° from the leading edge of the cylinder; (iii) a preliminary single-phase simulation is run until the temperature at the nucleation point reaches the nucleation temperature. Any variation to this procedure will be explained in the relevant sections of this article.

Once the initial conditions are identified, the boiling process in the two-phase simulation is initiated by seeding a spherical bubble of initial diameter of 10 μm at the nucleation point. The temperature within the bubble is set to T_{sat} and the fluid velocity to zero. The two-phase simulation then evolves in time until the bubble reaches the outlet section of the channel, which takes about 1 millisecond; the time-step of the simulations ranged from 10^{-8} s to 10^{-7} s.

4. Mesh convergence analysis

The mesh convergence analysis was performed for a representative case run with inlet restrictions, $G = 1000\,\mathrm{kg/(m^2s)}$, $q = 200\,\mathrm{kW/m^2}$, $T_{sat} = 30\,°\mathrm{C}$ and no inlet subcooling. The computational domain utilised is analogous to that depicted in Fig. 1(b); it incorporates two rows of pin-fin arrays with their adjacent channels ($W = 300\,\mu\mathrm{m}$), and it has a length of 2.1 mm, corresponding to about 20 pin-fins being modelled in the streamwise direction.

Table 2
Details of the three computational grids tested, characterised with the number of cells per cylinder radius in the bulk flow region (R/Δ), number of recursive refinements near the cylinders walls (n), and smallest size of the cubic cells in the refined region $\Delta_{min} = \Delta/2^n$.

Mesh convergence analysis				
Mesh	R/Δ	n	cells number	$\Delta_{min} = \Delta/2^n$
M1	7.5	2	5 841 352	$0.033R = 0.83\,\mu\mathrm{m}$
M2	10	2	11 101 302	$0.025R = 0.62\,\mu\mathrm{m}$
M3	12.5	2	18 557 950	$0.02R = 0.5\,\mu\mathrm{m}$

The domain is discretised with an arbitrary polyhedral grid structure with mainly hexahedral elements. The domain is meshed in two successive steps, using OpenFOAM's tool snappyHexMesh. First, the entire domain block with no pin-fins is meshed using uniform cubes with cell size Δ. Then, the mesh is recursively refined $n = 2$ times near the cylinder surface by splitting a cube into eight smaller cubes for each refinement cycle. Finally, the cubes are clipped to fit the surface of the cylinders and the cylinders are subtracted from the computational domain. Three meshes were tested, starting with different values of the largest cubic cells. The representative parameters of the mesh are listed in Table 2, and a close-up view of the mesh near one pin-fin is shown in Fig. 2(a). Note that for all meshes employed in the grid independence analysis, the smallest cell near the cylinder surface has a size below 1 μm.

The identification of the suitable initial conditions for the simulation follows the procedure outlined in Section 3.3. For $G = 1000\,\mathrm{kg/(m^2s)}$ and $q = 200\,\mathrm{kW/m^2}$, Falsetti et al. [18] measured a heat transfer coefficient of about $12.5\,\mathrm{kW/(m^2K)}$ at zero vapour quality, which corresponds to a nucleation superheat of 16 K and a wall temperature of 319 K. Therefore, the preliminary single-phase simulation is run until the temperature at the nucleation point reaches this value, after which a small bubble is seeded and the two-phase simulation begins.

Upon boiling onset, the bubble grows quickly due to the superheated liquid surrounding the cylinder. Fig. 2(b) and (c) display the temporal evolution of the velocity of the bubble nose and the bubble length as the bubble grows and accelerates downstream the evaporator. Both bubble speed and length increase over time and achieve a linear trend as a function of the position of the bubble nose in agreement with those observed for bubbles propagating in straight microchannels [38,39]. The presence of the cylinders acting as periodic obstacles for the flow of the bubble is manifested in Fig. 2(b) by the periodic oscillations of the bubble nose speed. The bubble dynamics and heat transfer for this case will be analysed in detail in Section 5.2. All computational grids tested yield similar values of bubble speed and length, with a systematic trend towards lower evaporation rates as the mesh is refined, which was already previously observed in boiling simulations employing the phase-change model of Hardt and Wondra [32]. Nonetheless, the relative differences between the equivalent bubble diameters at the end of the simulations for the different grids, plotted in Fig. 2(d), is less than 7%. This suggests that all grids capture the bubble dynamics well. Fig. 2(e) shows the average surface temperature and Nusselt number ($\mathrm{Nu} = q d_h/[\lambda_l(\overline{T_s} - T_{sat})]$), calculated as a spatial average over all heated surfaces (base and pin-fins). The differences between the three meshes are minimal, with mesh M2 ($R/\Delta = 10$) exhibiting a temporally-averaged Nusselt number which is only 3% smaller than M1 ($R/\Delta = 7.5$), and less than 3% higher than that measured with the finest mesh M3. The instantaneous values of average temperature and Nusselt number at the end of the simulation are also very similar, with less than 5% difference between M2 and M3. Hence, mesh M2 was the mesh used

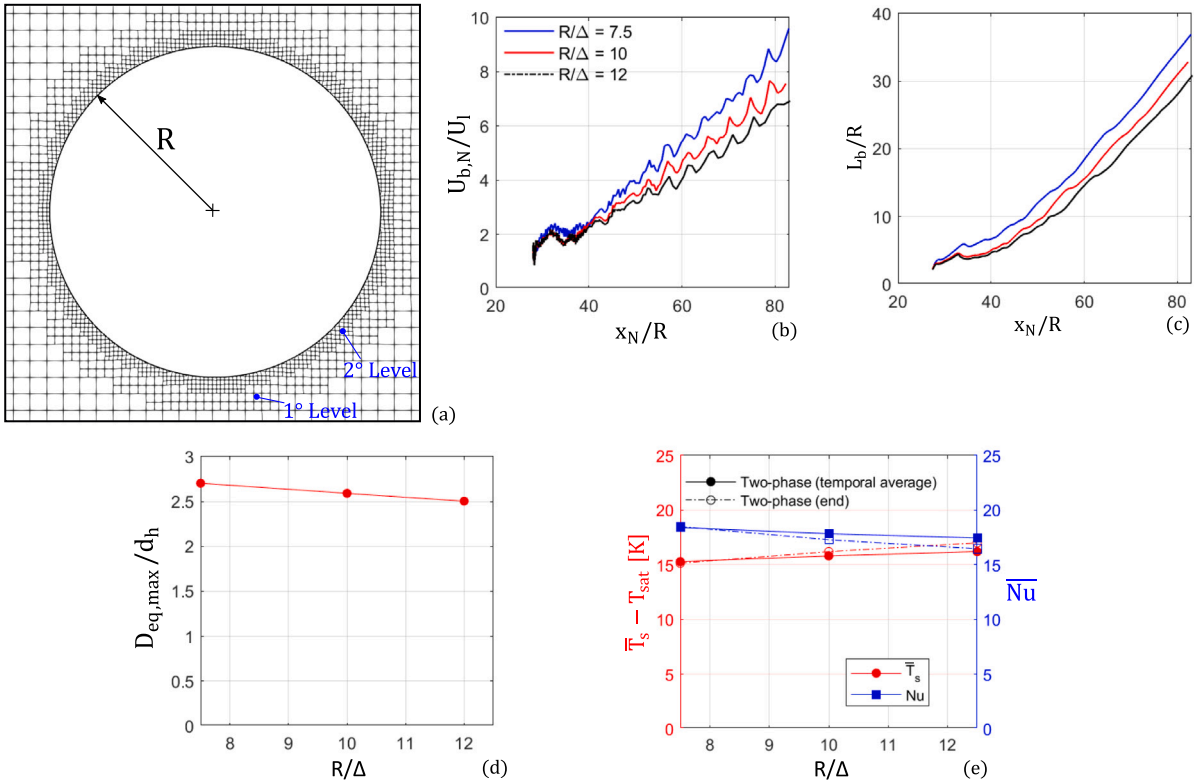

Fig. 2. Results for the mesh convergence analysis. (a) Example of computational mesh near a cylinder, for a grid arrangement with $R/\Delta = 10$ and $n = 2$ (mesh M2 in Table 2). (b–c) Evolution of the bubble nose velocity and bubble length while the bubble flows downstream the channel; x_N indicates the streamwise location of the bubble nose. The legend in (b) applies also to (c). (d) Maximum bubble equivalent diameter at the instant when the bubble approaches the outlet section, rescaled by the channel hydraulic diameter, $d_h = 100\,\mu m$. (e) Spatially-averaged temperature ($\overline{T}_s$) and Nusselt number ($\overline{Nu}$) of the heated surfaces (heater and pins). The data are presented as a time-average over the entire simulation and as an instantaneous value at the end of the simulation. The results refer to a case run with inlet restrictions, $G = 1000\,kg/(m^2s)$, $q = 200\,kW/m^2$, $T_{sat} = 30\,°C$ and no inlet subcooling.

to perform the simulations presented in the next sections. Simulations were run on the high-performance computing cluster Sulis (https://warwick.ac.uk/research/rtp/sc/sulis). Using typically 128 cores and OpenFOAM's scotch domain decomposition, the computational time for each simulation ranged from 5000 (low Re) to 7000 CPU hours (high Re).

5. Results

The results of this work are presented below, organised in subsections. Section 5.1 reports the results of a validation study. Section 5.2 presents a detailed analysis of the two-phase hydrodynamics and heat transfer for one representative case. The effect of the inlet flow rate is analysed in Section 5.3. Section 5.4 describes the simulation results performed by changing the nucleation site location. The last Section 5.5 illustrates the analysis of the effect of the inlet subcooling.

5.1. Validation

5.1.1. Single-phase validation

The numerical framework was first validated versus the single-phase pressure drop and heat transfer data obtained by Falsetti et al. [18]. The authors performed single-phase experiments at low heat fluxes to validate their experimental and measurement setup against established correlations for friction factor and Nusselt number across pin-fins and tube banks. In this work, single-phase numerical simulations were run on a domain of length of 1 cm, coinciding with the experimental setup, but modelling only one row of pin-fins and the adjacent channels ($W = 150\,\mu m$). Simulations were performed by varying the mass flux in the range $G = 500$–2500 kg/(m^{2}s), while keeping the heat flux fixed at $q = 50\,kW/m^2$, until velocity and temperature fields achieved steady-state regimes for each flow rate. The Reynolds number is calculated using the hydraulic diameter of the straight channel formed between the pin-fin arrays, $d_h = 100\,\mu m$, in agreement with Falsetti et al. [18]:

$$Re = \frac{G d_h}{\mu_l} \tag{9}$$

The range of Reynolds numbers corresponding to $G = 500$–$2500\,kg/(m^2s)$ is $Re = 187 - 935$.

The results of the single-phase validation study are presented in Fig. 3. Fig. 3(a) shows the pressure profile along the channel centreline ($y = 0$, $z = H/2$) for different mass fluxes, while Fig. 3(b) shows the corresponding velocity and pressure fields near the inlet. The pressure profiles reveal a sudden pressure drop immediately after the larger pin serving as inlet restriction, followed by a gradual pressure recovery. For $G = 500\,kg/(m^2s)$, the pressure increase due to pressure recovery is approximately 100 Pa, extending over a length of $x \approx 12R$. For $G = 2500\,kg/(m^2s)$, the pressure increase is 2700 Pa, extending over a length of $x \approx 40R$. At low values of the mass flux, $G < 1000\,kg/(m^2s)$ ($Re < 374$), the flow field achieves steady-state along the whole length of the evaporator. The recirculating regions downstream each pin-fin remain stationary and form two sets of counter-rotating vortices; see, for example, Fig. 3(c), where streamlines are reported on a horizontal mid-plane ($z = H/2$) far from the inlet section ($x/R \approx 200$). Steady recirculating patterns for flow past cylinders at Reynolds numbers much larger than 100 in the presence of strong confinement were also reported by Zhang et al. [42]. At $G = 1000\,kg/(m^2s)$, some weak unsteadiness on the flow in the pin-fins wake becomes apparent, which gives rise to asymmetric wakes. However, the recirculating region remains bounded in the gap between consecutive cylinders. The flow field always reaches nearly steady-state conditions for $G < 2000\,kg/(m^2s)$,

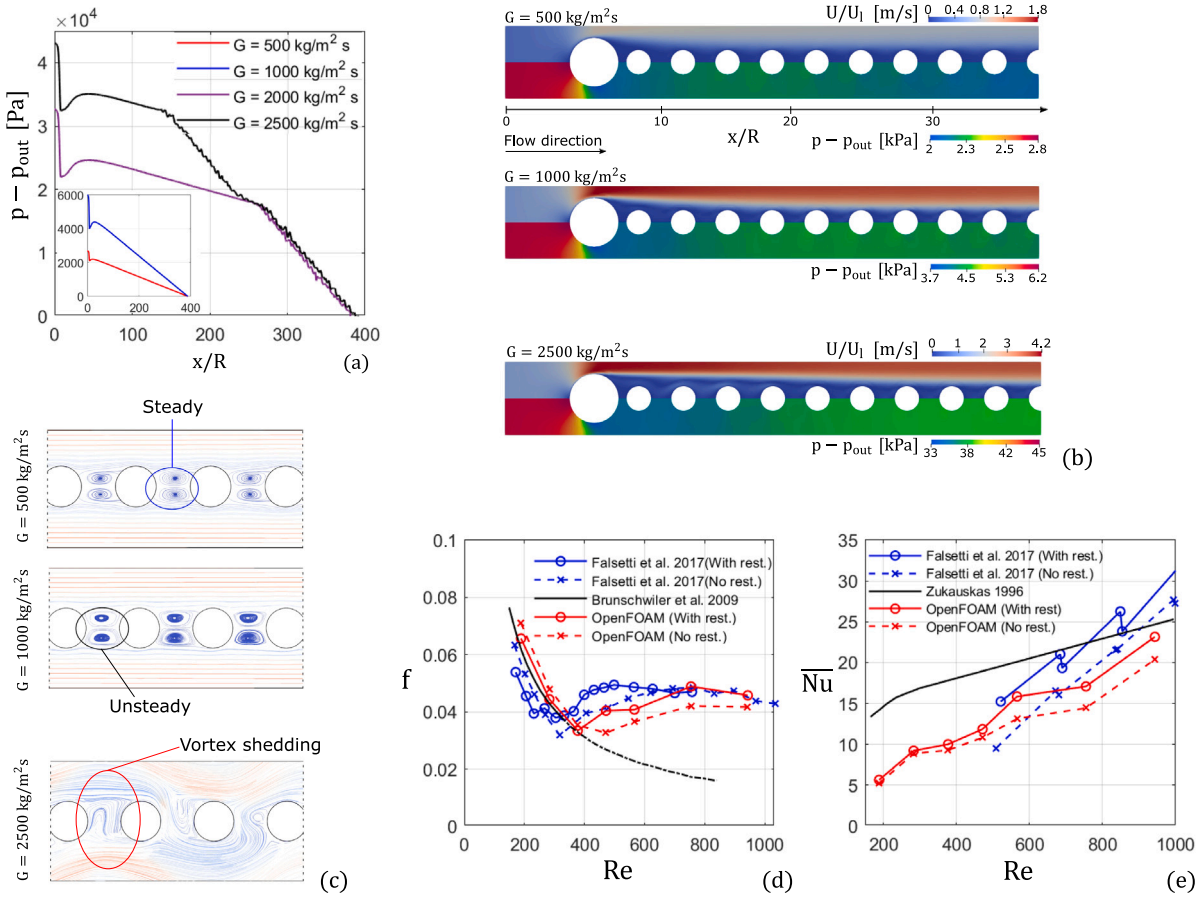

Fig. 3. Results of the single-phase validation study. (a) Axial pressure profiles extracted along the centreline of the channel formed between the pin-fin arrays ($x, y = 0, z = H/2$). (b) Snapshots of velocity (top half) and pressure contours (bottom half), extracted at steady-state in the mid-height plane ($z = H/2$) near the inlet section for different mass fluxes at the inlet. (c) Flow streamlines for different values of G, farther from the inlet section ($x/R \approx 200$). (d) Single-phase friction factor as a function of the liquid Reynolds number for geometries with and without inlet restrictions. As a reference, the chart presents also the friction factor data reported by Falsetti et al. [18] and the f prediction using Brunschwiler et al. [40] correlation. (e) Spatially-averaged Nusselt number of the heated surfaces (heater and pins) at steady-state versus Reynolds number for both geometries. As a reference, the graph contains also the Nusselt number results of Falsetti et al. [18] and the predictions for tube bundles using Zukauskas [41] correlation.

and the axial pressure profile exhibits a uniform linear decay along x as observed for $G = 500\,\mathrm{kg/(m^2s)}$ and $1000\,\mathrm{kg/(m^2s)}$ in Fig. 3(a). As the mass flux is increased to $G = 2000\,\mathrm{kg/(m^2s)}$, to which it corresponds $\mathrm{Re} = 748$, strong vortex shedding begins appearing from a certain axial location in the evaporator, $x/R \approx 270$, see Fig. 3(c). The transition to the vortex shedding regime induces a significant change in trend in the axial pressure profiles displayed in Fig. 3(a), causing a sharp change in the slope of the curve and thus increasing the pressure drop. Upon a further increase of the mass flux to $G = 2500\,\mathrm{kg/(m^2s)}$, the slope of the pressure profile does not exhibit significant changes. However, the transition to vortex shedding occurs earlier within the evaporator, and thus the total pressure drop increases considerably.

In the experiments of Falsetti et al. [18], the total pressure drop Δp_{tot} in the test section was measured using a differential pressure transducer between the inlet and outlet manifold plenums. To obtain the pressure drop along the pin-fin array, Δp_{fin}, they subtracted the contributions of the inlet and outlet pressure drop Δp_{in} and Δp_{out} from Δp_{tot}, so that $\Delta p_{fin} = \Delta p_{tot} - \Delta p_{in} - \Delta p_{out}$. The inlet pressure drop Δp_{in} was estimated by summing the contributions of two sudden contractions from the inlet manifold plenum to the test section inlet plenum, a third contraction across the inlet restrictions, and subtracting the pressure recovery due to the sudden expansion after the restrictions. The outlet pressure drop Δp_{out} was estimated by summing up the pressure recoveries due to three sudden expansions from the channels outlet to the outlet manifold plenum. All these seven contributions were calculated using empirical correlations [43]. From Δp_{fin}, the friction factor for the pin-fin array was calculated as follows:

$$f = \frac{\Delta p_{fin} \rho_l d_h}{2 L_c G^2} \tag{10}$$

The uncertainty on the friction factor was calculated using the Kline and McClintock method of propagation of error and returned a value of ±15%. However, the uncertainties introduced by the use of correlations to estimate the inlet and outlet pressure drops were not included. The correlations were originally developed for sudden restrictions and expansions within long channels, as such their use to estimate pressure drops in configurations where the flow cannot become fully developed between consecutive area changes, is expected to constitute another source of error. By estimating as 25% the uncertainty associated to each predicted contraction and expansion pressure drop, the overall uncertainty in the friction factor increases to about 20%. For a coherent comparison with the experiment, where the contribution of the pressure recovery after the inlet restrictions was incorporated into Δp_{in} (and thus excluded from Δp_{fin}), the friction factor in the simulations is calculated by considering as Δp_{fin} the pressure drop between the local maximum in pressure after the restrictions and the channel outlet.

The values of the friction factor for experiments and simulations are reported in Fig. 3(d). Evaporators with and without inlet restrictions were tested by Falsetti et al. [18] and the results for both configurations are included in Fig. 3(d). The figure includes also predictions obtained using an empirical correlation developed by Brunschwiler et al. [40] for water flowing across in-line circular pin-fins; this was developed by fitting experimental data measured at Reynolds numbers below 300,

and thus the curve for Re > 300 is displayed as a dashed line. Trends and magnitudes of the friction factor in experiments and simulations are in good agreement across the entire range of flow rates examined, with deviations that remain always below the uncertainty in the experimental values. The friction factor first reduces upon an increase in the Reynolds number. In the experiment, this trend exhibits a transition at about Re = 200–400, after which f slightly increases reaching a value of f = 0.045–0.05 that becomes approximately independent of Re. This transition was attributed to the establishment of vortex shedding in the wake of the pin fins. The friction factor in the simulations exhibits the same trend, with the transition in f occurring at Re = 400. Analysis of the flow patterns in the simulations confirms that the change of trend in f happens when the vortices in the wake of the cylinders become unsteady. As the flow rate is further increased, such that full vortex shedding is established, the friction factor attains asymptotically constant values which are weakly dependent on Re. Since in the simulations the inlet boundary condition sets a perfectly unidirectional flow at the test section inlet, it is reasonable that flow instabilities occur at slightly higher Reynolds number than the experiment, where the flow enters the channels after a series of changes in direction and cross-sectional area.

The results presented in this work were performed without using any turbulence model in the simulations. This is justified by the relatively small Reynolds number and by the fact that turbulence models for interface-resolved two-phase simulations are not well established. Single-phase flow past a cylinder may become weakly turbulent at the highest flow rates tested in this work, however, the flow model adopted is expected to remain suitable provided that the mesh is sufficiently fine to capture the smallest scales of the flow. The Kolmogorov scale η associated to the flow past the cylinders can be estimated as $\eta/D = \mathrm{Re}_D^{-3/4}$, with D being the diameter of the pin-fins and $\mathrm{Re}_D = GD/\mu_l$. This yields $\eta = 0.5\,\mu\mathrm{m}$ at the highest flow rate tested, which is on the order of the smallest cell size near the cylinders surface, as such it is expected that the smallest flow structures are captured by the mesh. Furthermore, the results of the mesh independence analysis and the good agreement between the experimental and computational values of the friction factor across the range of flow rates tested, provide confidence that the present numerical setup is sufficiently accurate to model the flow configuration under investigation.

For the experimental validation of the heat transfer performance, the average Nusselt number ($\overline{\mathrm{Nu}}$) is calculated from the numerical results. Following common practice for flow across banks of tubes [44,45], the Nusselt number in the simulations is calculated from a wall heat transfer coefficient which is computed by dividing the heat flux by the log-mean temperature as follows:

$$\overline{\mathrm{Nu}} = \frac{\overline{h}_w d_h}{\lambda_l}, \qquad \overline{h}_w = \frac{q}{\Delta T_{LM}} \tag{11}$$

where $\overline{h}_w$ is the average wall heat transfer coefficient and ΔT_{LM} is the log-mean temperature difference:

$$\Delta T_{LM} = \frac{T_{out} - T_{inl}}{ln\left(\frac{\overline{T}_s - T_{inl}}{\overline{T}_s - T_{out}}\right)} \tag{12}$$

where T_{out} is the average bulk temperature measured at the outlet, T_{inl} is the average bulk temperature at the inlet and $\overline{T}_s$ is the average temperature of the heated walls (base evaporator wall and pin-fins). The use of the log-mean temperature instead of the temperature difference becomes important in particular at low Re, where the fluid may experience a large change in temperature as it moves through the pin-fin arrays [45]. The results are reported in Fig. 3(e), where the average single-phase Nusselt number ($\overline{\mathrm{Nu}}$) is plotted as a function of Re. The graph also includes the experimental results of Falsetti et al. [18] and the Nu predicted using Zukauskas correlation for tube bundles [41]. The results exhibit an approximately linear trend versus the Reynolds number and are in good agreement with the experimental data, both with and without inlet restrictions. The heat transfer performance increases with a higher Reynolds number, which is expected due to the promotion of the flow mixing and generation of vortex shedding along the channel. Experimental and computational Nusselt numbers match very well for Re = 500 – 600, whereas for higher flow rates the simulations underpredict the experimental data by about 15%, which is on the order of the experimental uncertainty on $\overline{\mathrm{Nu}}$. This deviation may be also due to the different data reduction procedures adopted to obtain heat transfer coefficients from raw data. The log-mean temperature difference method is used in the simulation, which is common practice for fluid flow across tube banks. In the experiment, the wall temperature was calculated from the two-dimensional temperature and heat flux maps measured on the outer surface of the evaporator base by infrared thermography. An inverse three-dimensional heat conduction problem was then solved to estimate the footprint heat transfer coefficient and Nusselt number. This indirect measurement method is likely affected by an additional uncertainty that cannot be quantified.

5.1.2. Two-phase validation

A flow boiling simulation at conditions matching one selected configuration from Falsetti et al. [18] was performed to validate the two-phase numerical setup. The simulation is run for an evaporator with inlet restrictions, $G = 1000\,\mathrm{kg/(m^2 s)}$, $q = 200\,\mathrm{kW/m^2}$, $T_{sat} = 30\,^\circ\mathrm{C}$. Two arrays of pin-fins with their adjacent channels are included in the numerical model, with the domain length limited to 2.1 mm to maintain an affordable computational cost. As initial condition, a small vapour bubble is generated on the fifth pin-fin when the local temperature reaches 319 K, as explained in Section 3.3. In the experiment, boiling gives rise to the nucleation of multiple bubbles and this behaviour must somehow be reproduced for a coherent comparison of heat transfer coefficients. The bubble generation frequency is not known from the experiment, however, Falsetti et al. [46] estimated it to be within the range 6000 – 8000 1/s for R236fa in the conditions under investigation. Hence, the validation simulation was run by generating bubbles from the same nucleation spot with a frequency of 7000 1/s, corresponding to a time interval of 0.14 ms between the nucleation events. It takes about 1 ms for the generated bubbles to reach the outlet of the channel, as such there are always about 4–5 bubbles simultaneously present in the simulated domain. Since the outlet boundary condition becomes unsuitable when bubbles are crossing the outlet boundary, bubbles are eliminated as soon as they reach the outlet section. This way, the numerical model is able to reproduce a continuous two-phase flow within the channels.

The spatially-averaged wall heat transfer coefficient obtained in the two-phase simulation is plotted as a function of time in Fig. 4. The figure also includes the benchmark value measured in the experiment [18] for vapour qualities in the range 0–0.05, $\overline{h}_{w,exp} = 12300\,\mathrm{W/(m^2 K)}$, which corresponds to the bubbly-slug flow regime simulated. The yellow area in the figure identifies the uncertainty in the experimental value, which was calculated as 12%. At the onset of the two-phase simulation, the heat transfer coefficient is higher than the experiment owing to the initial condition set. As time elapses, the heat transfer coefficient decreases because the wall is still heating up, however, as the two-phase flow develops and more bubbles are generated, the surface area covered by the bubbles increases benefitting heat transfer. The sequential generation and removal of bubbles as they reach the outlet induces a periodic trend on the heat transfer coefficient versus time as observed in Fig. 4. The heat transfer coefficient tends to an asymptotically steady-periodic trend with average value of about $\overline{h}_w = 11800\,\mathrm{W/(m^2 K)}$ in the simulation, which agrees well with the experiment as deviations remain well within the experimental uncertainty.

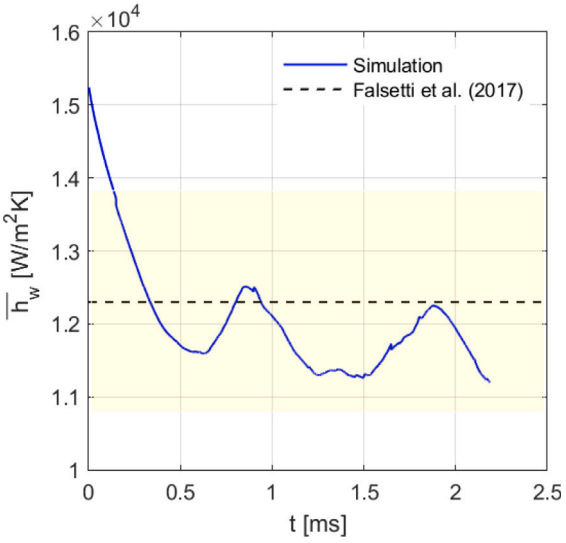

Fig. 4. Results of the two-phase validation study. The conditions simulated are $G = 1000\,\mathrm{kg/(m^2s)}$, $q = 20\,\mathrm{W/cm^2}$, $T_{sat} = 30\,^{\circ}\mathrm{C}$, evaporator with inlet restrictions. The time-dependent spatially-averaged heat transfer coefficient of the heated surfaces (heater and pins) from the simulation is compared to corresponding data from the experiments of Falsetti et al. [18]. The yellow band identifies the ±12% uncertainty in the experimental value. (For interpretation of the references to colour in this figure legend, the reader is referred to the web version of this article.)

5.2. Base case

In this section, we provide a detailed analysis of the results obtained for a reference case run with inlet restrictions, $G = 1000\,\mathrm{kg/(m^2s)}$, $q = 200\,\mathrm{kW/m^2}$, $T_{sat} = 30\,^{\circ}\mathrm{C}$ and no inlet subcooling; this was the case used for the mesh independence study in Section 4. The bubble nucleation point is set on the fifth cylinder, at 135° from the stagnation point at the cylinder upstream as indicated in Fig. 1(c). The nucleation temperature is set to 319 K as explained in Section 3.3. Unlike the two-phase validation study discussed in Section 5.1.2, only one bubble was nucleated in the simulations described in the remainder of this article.

The discussion will primarily focus on the following aspects: the development of the bubble shape, the flow dynamics, the morphology of the liquid film thickness and the heat transfer performance of the micro-pin-fin evaporator. Fig. 5(a) shows the evolution of the bubble equivalent diameter as time elapses and panels (b) and (c) illustrate corresponding bubble shapes at selected time instants during the simulation. The bubble equivalent diameter is calculated at each time-step as the diameter of a spherical bubble of volume equivalent to that of the simulation. When the ratio of equivalent diameter to channel hydraulic diameter, D_{eq}/d_h, grows above 1, the bubble becomes strongly confined by the channel walls. As the bubble nucleates (instant A), it grows very rapidly in size owing to the superheat accumulated by the liquid in the neighbourhood of the nucleation spot, which is the hottest zone of the evaporator due to the recirculating fluid in the cylinder wake. The bubble departs quickly from the cylinder where it nucleated due to the drag exerted by the incoming liquid and migrates towards the centre of the channel (instants B and C). Its growth rate subsides during this stage due to the cooler liquid far from the heated surfaces. At about $t = 0.4$ ms (instant D), the bubble has grown in size to occupy the whole channel cross-section and comes in contact with the second array of cylinders (in $y < 0$). At this point, the growth of the bubble is restricted by the pin-fins, which act as bounding walls, the bubble predominantly expands in the flow direction and tends to elongate as observed in straight channels [34]. However, unlike straight channels, the bubble tends to expand also in the width-wise cross-stream direction in the gap between the cylinders. These are hot regions in the evaporator, and thus the sensible heat accumulated in the recirculating fluid in the wakes of the cylinders directly contributes to the evaporation rate of the bubble. Fig. 5(d) depicts the bubble, the velocity and temperature contours extracted on a horizontal mid-plane $z = H/2$ at instant E, shortly before the bubble nose reaches the end of the channel. It is interesting to observe that the expansion of the bubble in the gap between the cylinders pushes liquid sideways, away from the cylinder wake. This is not only hot liquid from the stagnation zone but also cooler liquid draining out of the thin liquid film region trapped between the pin-fins and the bubble interface. El Mellas et al. [26] showed that the capillary pressure gradient established between the concave bubble region indented by the cylinder, where pressure is higher, and the convex region formed in the gap between two cylinders, where pressure is lower, causes continuous drainage of the thin film trapped between bubble and cylinder. This drainage flow, emphasised with the red ellipses in Fig. 5(d), is composed of cooler liquid at near-saturation conditions due to the thin-film evaporation process, which is manifested by the blue streaks apparent in the temperature contours of Fig. 5(d).

To further illustrate the bubble dynamics during its growth, Fig. 6 displays selected profiles of the liquid–vapour interface and temperature field extracted at the time instants labelled as D and E in Fig. 5. For each time instant, the figures show the interface profiles and temperature contours on the vertical mid-plane at $y = 0$ and two selected cross-sectional $y - z$ planes. The two cross-stream planes for each time instant are chosen to be in a region occupied by the bubble ($x/R = 38 - 42$ for instant D; $x/R = 50 - 78$ for E), with one plane centred on a specific cylinder and a second plane located half-way between the same cylinder and the previous one. For time instant D, the selected cylinder is the 9th, corresponding to the planes $x/R \approx 38$ and 40. For time instant E, the selected cylinder is the 15th, corresponding to $x/R \approx 60$ and 62. Surface tension forces, together with the effect of the evaporation, redistribute the liquid surrounding the bubble into thin films covering the cylinders and the top and bottom channel walls, similar to what is observed in square channels [23]. At time instant D, the bubble is not large enough to completely fill the channel and the bubble's cross-sectional shape is still approximately circular, see Fig. 6(a) and (b), with the minimum film thickness being detected in the correspondence of the half-height of the channel ($z = H/2$) on the cylinders' surface. As the bubble grows and fills the channel cross-section, the film changes its shape; see instant E in Fig. 6(c) and (d). The liquid film becomes thinner, which can be attributed to the gradual evaporation and drying out of the film over time. The position of the minimum film thickness from the mid-height shifts towards the top and bottom walls, where two dimples appear, identifying two minimum film thickness regions. Where it is not constrained by the fins, the bubble expands remarkably in the cross-stream direction until about $y/R = \pm 3$, and film evaporation contributes to the cooling of the heater surface in the gap between the cylinders.

To better analyse the impact of the two-phase flow on heat transfer, Fig. 7(a,b) provides axial profiles of temperature and Nusselt number, both averaged for each pin-fin. These profiles were extracted at different time instants, as indicated in Fig. 5(a). The solid markers represent the pin-fins on the side of positive y of the geometry, where the bubble is initially positioned, while the empty markers represent the pin-fins on the opposite side ($y < 0$). Note that at instant A (boiling onset), the two arrays of pin-fins have the same temperature, and thus a single set of symbols (crosses) is used. The chart also includes time-averaged results obtained from the entire two-phase simulation. As time elapses, temperatures increase, and thus Nusselt numbers decrease as the evaporator heats up over time. The highest temperature is detected on the second set of pin-fins, right after the inlet restriction, because the restriction generates a large recirculation region. During the initial stages, when the bubble equivalent diameter is smaller than or on the order of the channel hydraulic diameter (instants B, C and D), the increase of the Nusselt number brought by the two-phase flow is still marginal and mostly felt only by the array of cylinders where

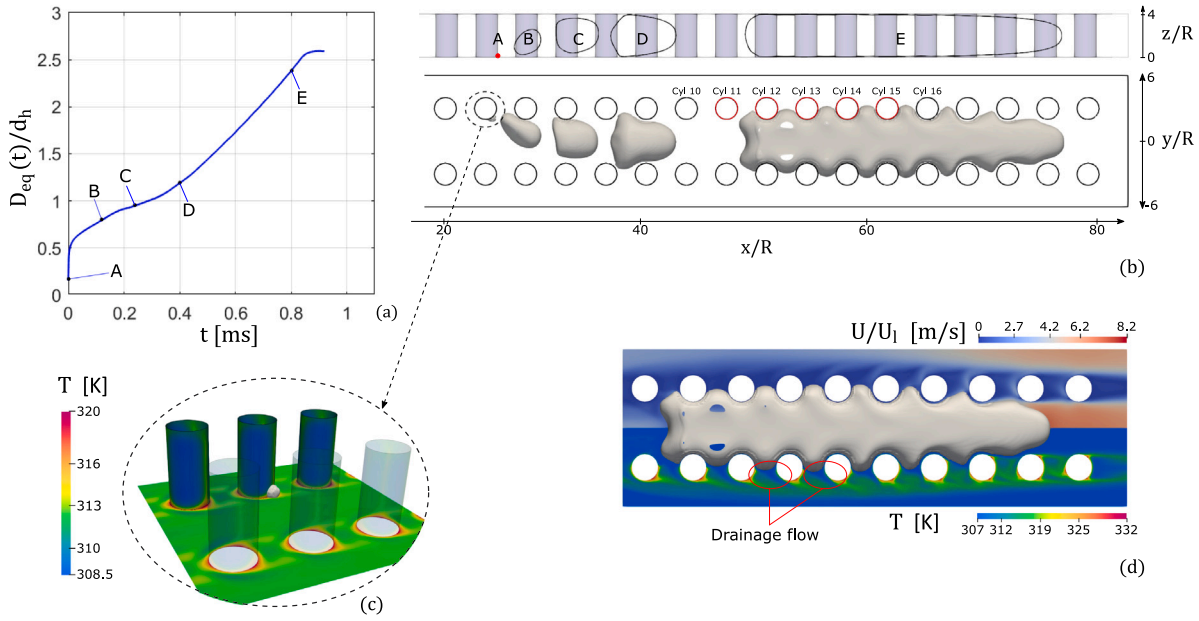

Fig. 5. Results for a reference case run with inlet restrictions, $G = 1000\,\mathrm{kg/(m^2 s)}$, $q = 200\,\mathrm{kW/m^2}$, $T_{sat} = 30\,^{\circ}\mathrm{C}$ and no inlet subcooling. (a) Dimensionless bubble equivalent diameter versus time. (b) Liquid–vapour interface profiles on a vertical mid-plane $y = 0$ and top view of the bubble profile extracted at the different instants indicated in (a). (c) Close-up view near the nucleation site of the bubble, in grey, and temperature contours of the cylinders and heater taken at the boiling onset. (d) Bubble profile, velocity (top half) and temperature (bottom half) on a horizontal mid-plane ($z = H/2$), extracted at the time instant E. (For interpretation of the references to colour in this figure legend, the reader is referred to the web version of this article.)

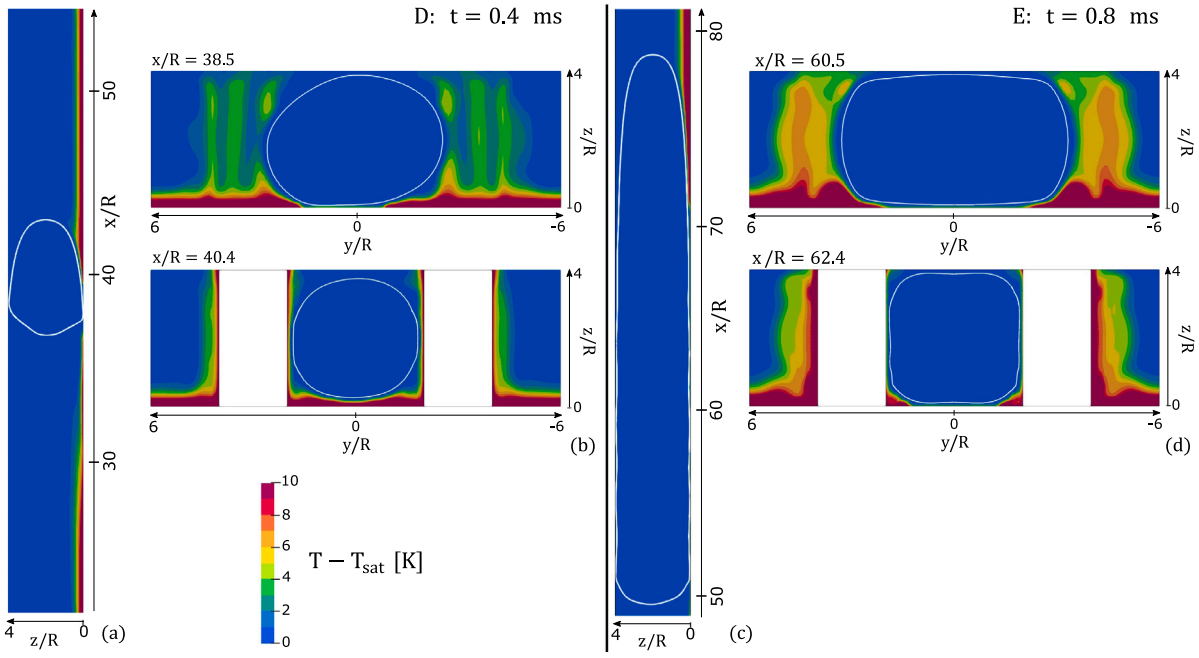

Fig. 6. Results for the reference case run with inlet restrictions, $G = 1000\,\mathrm{kg/(m^2 s)}$, $q = 200\,\mathrm{kW/m^2}$, $T_{sat} = 30\,^{\circ}\mathrm{C}$ and no inlet subcooling. (a) Liquid–vapour interface profiles and temperature contours on a vertical mid-plane $y = 0$ extracted at the time instant D. (b) Liquid–vapour interface profiles and temperature contours on the cross-section at planes $x/R \approx 38$ and 40, extracted at the time instant D. (c–d) Liquid–vapour interface profiles and temperature contours on the vertical mid-plane $y = 0$ and cross-sections on planes $x/R \approx 60$ and 62, extracted at the time instant E.

nucleation occurs. At the stage when the bubble is elongated (instant E), the beneficial effect of the two-phase flow is considerable and the pin-fin Nusselt number grows from about $\overline{\mathrm{Nu}}_{pin} = 16.5$ in the single-phase region of the channel to $\overline{\mathrm{Nu}}_{pin} = 25$ in the region occupied by the bubble and by the thin evaporating liquid film. At this stage, the cooling effect is relatively uniform between the two arrays of cylinders. The time-average Nusselt number reported with red squares in Fig. 7(b) emphasises the beneficial effect of the two-phase flow in causing a localised increase of the heat transfer performance in the region of the evaporator covered by the elongated bubble, as exemplified by the monotonically increasing trend of $\overline{\mathrm{Nu}}_{pin}$ along the evaporator. A qualitatively similar heat transfer trend was observed by Falsetti et al. [18]

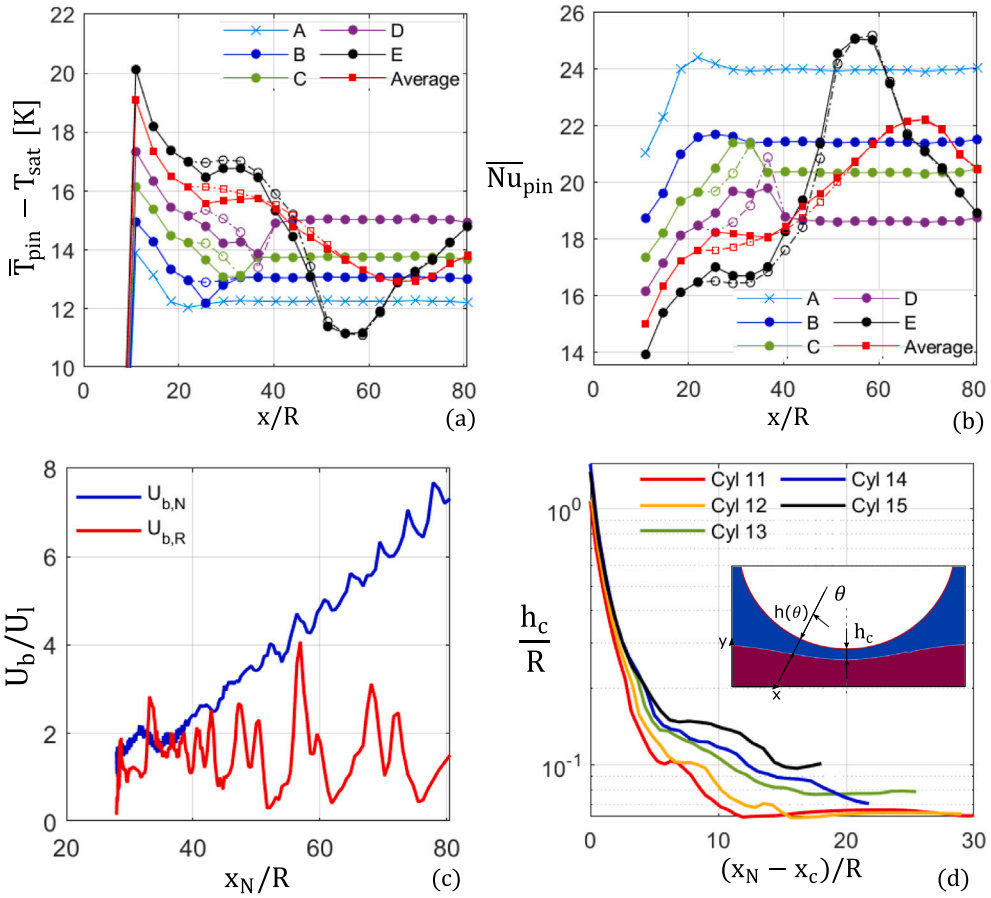

Fig. 7. Results for the reference case run with inlet restrictions, $G = 1000\,\mathrm{kg/(m^2s)}$, $q = 200\,\mathrm{kW/m^2}$, $T_{sat} = 30\,^{\circ}\mathrm{C}$ and no inlet subcooling. (a-b) Instantaneous two-phase spatially-averaged temperature ($\overline{T}_{pin}$) and Nusselt number ($\overline{\mathrm{Nu}}_{pin}$) of the pin-fins over the streamwise direction, taken at the time instants indicated in Fig. 5(a). The full markers indicate the results of the array of pin-fins on the side of positive y, where the bubble nucleates, while the empty markers refer to the array of pin-fins on the opposite side ($y < 0$). The graph also shows the time-average results during the entire two-phase simulation. (c) Evolution of the bubble nose ($U_{b,N}$) and rear ($U_{b,R}$) velocity as the bubble travels through the domain. (d) Evolution of the dimensionless liquid film thickness (h_c/R) while the bubble flows downstream, measured over the 11th to 15th cylinders; these were coloured in red in Fig. 5(b). The film thickness is plotted as a function of the bubble nose streamwise distance from the cylinders' centres, $x_N - x_c$. The inset provides a close-up view of the liquid film profile in a horizontal centreplane ($z = H/2$), near a cylinder, with the liquid and vapour regions coloured in blue and red, respectively. The liquid film thickness h_c is measured as the distance between the interface and the cylinder surface on a local reference frame centred on the cylinder centre. (For interpretation of the references to colour in this figure legend, the reader is referred to the web version of this article.)

under the same conditions ($G = 1000\,\mathrm{kg/(m^2s)}$, $q = 200\,\mathrm{kW/m^2}$), which was ascribed to the formation of extended evaporating film regions as the flow pattern developed from slug to annular flow.

Last, Fig. 7(c) and (d) report the bubble speed and thickness of the evaporating film formed over the pin-fins surfaces as the bubble grows downstream in the channel. The velocity of the bubble front and rear, denoted as $U_{b,N} = dx_N/dt$ and $U_{b,R} = dx_R/dt$, respectively, are shown as a function of the bubble nose position. Here, x_N and x_R represent the streamwise coordinates of the nose and rear tips of the bubble. The bubble does not reach a steady terminal velocity but experiences oscillations due to the influence of the pin-fins. The front of the bubble experiences higher velocities compared to the rear due to the evaporation process that makes the bubble longer as time elapses. The liquid film thickness h_c in Fig. 7(d) is measured as the distance between the liquid–vapour interface and the cylinder surface evaluated on a horizontal mid-plane ($z = H/2$) along a cross-stream y-axis passing through the cylinder centre, as sketched in the figure inset. The film thickness is plotted as a function of the axial distance of the bubble nose (x_N) from the centre of the cylinder (x_c). As the bubble nose flows past the cylinder, h_c decreases due to the combined effect of draining flows [26] and thin-film evaporation. The minimum film thickness values range from about $h_c = 0.06R$ to $0.1R$ (i.e. from 1.5 μm to 2.5 μm), with progressively thicker films being established on cylinders downstream the channel due to the rising speed of the bubble nose. These thicknesses compare well with those measured by El Mellas et al. [26] for isothermal flows at similar values of the bubble capillary number, $\mathrm{Ca_b} = \mu_l U_{b,N}/\sigma \approx 0.2$. The thin-film regions provide a remarkable contribution to heat transfer. The local Nusselt number can be estimated by assuming one-dimensional steady-state heat conduction across the film, such that the heat transfer coefficient is calculated as $h = \lambda_l/h_c$ and thus $\mathrm{Nu} = d_h/h_c$, which yields $\mathrm{Nu} = 40 - 67$ for $h_c = 1.5{-}2.5\,\mu\mathrm{m}$. This explains the sudden increase of $\overline{\mathrm{Nu}}_{pin}$ observed in Fig. 7(b) at instant E in the region where the thin liquid film is formed, i.e. $x/R = 50 - 60$. No liquid film dryout is observed on the pin-fins. The time necessary for evaporation to completely deplete the liquid film can be estimated as $t_{dry} = h_c \rho_l h_{lv}/q$, which yields $t_{dry} \approx$ 1.4–2.4 ms for h_c = 1.5–2.5 μm. Therefore, the time necessary for evaporation to dry the film is larger than the residence time of the film over the cylinder, which explains why dryout does not occur under the present conditions.

5.3. Effect of the mass flux

In this section, we investigate the impact of the mass flux on the two-phase dynamics and heat transfer performances. Within micro-heat exchangers, inertial forces can still be relevant despite the small channel sizes because the use of low-viscosity refrigerants and the need for efficient convective cooling may result in values of the Reynolds

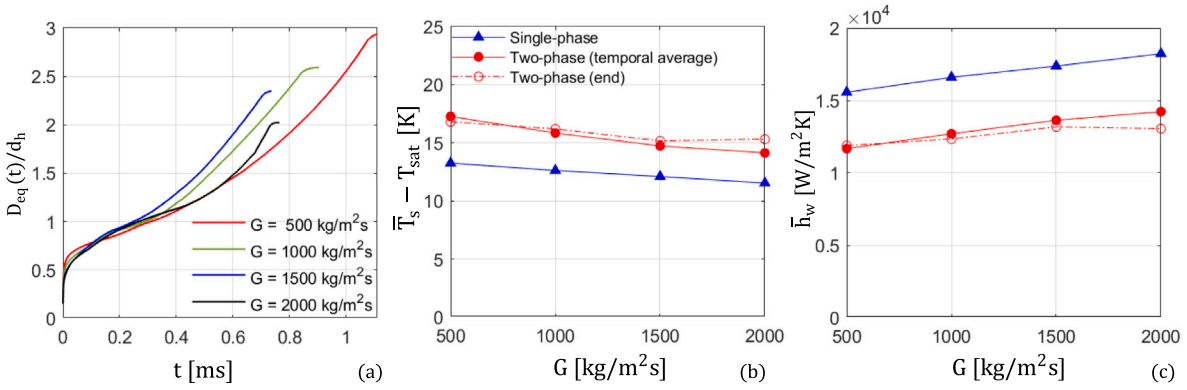

Fig. 8. Systematic analysis of the effect of the liquid mass flux at the inlet. (a) Dimensionless bubble equivalent diameter versus time. (b–c) Spatially-averaged single- and two-phase temperature ($\overline{T}_s$) and heat transfer coefficient ($\overline{h}_w$) of the heated surfaces (heater and pins). The single-phase data refer to the instant of boiling onset; for the two-phase results, data are presented as a time-average over the entire simulation and as instantaneous values at the end of the simulation, when the bubble nose reaches the outlet section. The legend in (b) applies also to (c). The results refer to a case run with inlet restrictions and $q = 200\,\mathrm{kW/m^2}$, $T_{sat} = 30\,^{\circ}\mathrm{C}$ and no inlet subcooling.

number approaching 10^3. Two-phase simulations are run for $G = 500, 1000, 1500, 2000\,\mathrm{kg/(m^2s)}$, $q = 200\,\mathrm{kW/m^2}$, and no inlet subcooling. Falsetti et al. [18] did not perform measurements for $G = 500\,\mathrm{kg/(m^2s)}$ and $G = 2000\,\mathrm{kg/(m^2s)}$, and thus the boiling onset temperature for the two-phase simulations cannot be estimated as explained in Section 3.3. To facilitate a comparison of the numerical results obtained at different flow rates, the nucleation temperature is set to 319 K for all cases, as it was calculated previously based on the experimental results with $G = 1000\,\mathrm{kg/(m^2s)}$.

The bubble equivalent diameter versus time for the different cases is displayed in Fig. 8(a). As the mass flux increases, the bubble growth rate during the early stages reduces due to the thinner thermal boundary layers established around the pin-fins. At larger time instants, Fig. 8(a) suggests that the growth rate increases with increasing mass flux for $G = 500{-}1500\,\mathrm{kg/(m^2s)}$, which is due to the fact that the bubble travels faster along the channel under the increased drag force exerted by the fluid, and thus it covers a larger heated area in the unit time resulting in higher evaporation rates. The bubble grows significantly less for $G = 2000\,\mathrm{kg/(m^2s)}$. This can be explained by the high shear force exerted by the incoming liquid that tends to detach the bubble from the hot cylinders already at early stages and by the reduced thickness of the thermal boundary layers that are feeding the liquid evaporation process. Further insight can be gained by inspection of the snapshots of the bubble dynamics at different mass fluxes provided in Fig. 9. For $G = 500\,\mathrm{kg/(m^2s)}$ and $G = 1000\,\mathrm{kg/(m^2s)}$ the process of bubble growth, departure from the nucleation point and elongation appear in a well-ordered sequence, with the bubble exhibiting a rounded rear meniscus and a slender front meniscus as expected in flows governed by capillary forces. Already at $G = 1500\,\mathrm{kg/(m^2s)}$, to which it corresponds a Reynolds number of the incoming liquid of $\mathrm{Re} = Gd_h/\mu_l = 561$, the process of bubble elongation begins when the bubble is smaller than the channel size due to the high-shear hydrodynamic boundary layers formed by the cylindrical obstacles. The bubble eventually grows to occupy the entire channel cross-section and elongates in the flow direction, although the rear meniscus loses the spherical shape observed at lower mass fluxes and wobbles as the bubble propagates downstream. This is due to the high inertial forces that tend to produce an unsteady dynamic of the tail of long bubbles, as already reported for slug flows in circular channels [47,48]. At the highest mass flux tested, $G = 2000\,\mathrm{kg/(m^2s)}$ (Re = 748), the high-shear forces overcome surface tension and cause high deformation and eventually fragmentation of the bubble. Owing to the thinner thermal boundary layers and the high fluid speed, the bubbles quickly reach the end of the channel without growing to a sufficient size to occupy the channel cross-section. Therefore, they are less in contact with the hot cylinder surfaces and are thus characterised by a reduced growth rate, which explains the trend observed in Fig. 8(a).

Fig. 8(b,c) presents the results of single- and two-phase spatially-averaged temperatures and heat transfer coefficients obtained for different mass flow rates. The single-phase data refer to the instant of boiling onset, whereas two sets of two-phase data are plotted, one averaged in time during the entire two-phase simulation, and one evaluated at the end of the two-phase simulation, when the bubble nose reaches the outlet section. Note that the two-phase temperatures are higher than the single-phase ones, with the heat transfer coefficients correspondingly lower, because the evaporator temperature increases over time. As a general trend, the heat transfer performances improve by increasing the mass flow rate, mainly due to the enhanced convective heat transfer between fluid and solid walls. However, the four-fold increase in mass flux from $G = 500\,\mathrm{kg/(m^2s)}$ to $G = 2000\,\mathrm{kg/(m^2s)}$ only results in a few per cent increase of the heat transfer coefficient, from $\overline{h}_w = 12\,\mathrm{kW/(m^2K)}$ to $\overline{h}_w = 14\,\mathrm{kW/(m^2K)}$ when considering time-averaged values in Fig. 8(c). Furthermore, this increasing trend seems to saturate as the mass flux approaches $G = 2000\,\mathrm{kg/(m^2s)}$, suggesting that a further increase in the mass flow rate may no longer improve two-phase heat transfer. This is related to the change in the two-phase flow pattern explained above with the aid of Fig. 9. Since the bubbles lose their bullet shape due to the high inertial forces and grow to a lesser extent due to the reduced contact time with the heated walls, the surface area of the evaporator covered by a thin evaporating film is significantly reduced, which has a detrimental impact on heat transfer.

A comparison with the trends observed by Falsetti et al. [18] at varying mass fluxes for the same heat load is difficult because non-monotonic trends of h_w versus G were reported, depending on the vapour quality. Nonetheless, in the low vapour quality range which applies well to the present simulations, they detected a generally increasing trend of h_w with G from $G = 750\,\mathrm{kg/(m^2s)}$ to $G = 1750\,\mathrm{kg/(m^2s)}$, in agreement with the trend of the present numerical simulations for $G < 2000\,\mathrm{kg/(m^2s)}$.

5.4. Effect of the location of the nucleation site

The position of the nucleation sites in an evaporator is not usually known beforehand, unless nucleation cavities are artificially manufactured. To investigate the effect of the nucleation site location on the bubble dynamics and two-phase heat transfer, we have tested different nucleation positions while keeping these constant conditions: $G = 1000\,\mathrm{kg/(m^2s)}$ and $q = 200\,\mathrm{kW/m^2}$, with no inlet subcooling. In the cases presented in the previous sections, the nucleation spot was set on the fifth pin-fin at an angle of $\theta = 135°$ from the leading edge of the cylinder. Here, we tested $\theta = 0$, which coincides with the upstream stagnation point on the cylinder surface, its diametrically opposed downstream point $\theta = 180°$, and $\theta = 90°$ which is outside of

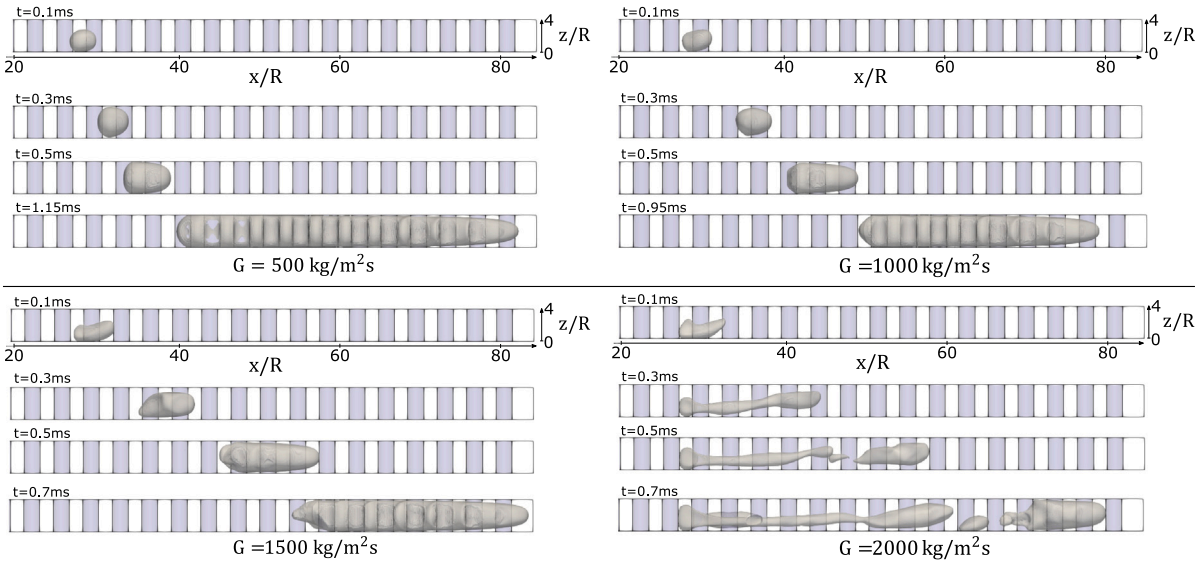

Fig. 9. Side view of snapshots of bubble growth for different values of the liquid mass flux at the inlet. To aid visualisation, the array of pins in $y < 0$ is removed. The figures show the bubble contour in grey and the cylindrical pin-fins are depicted in violet. (For interpretation of the references to colour in this figure legend, the reader is referred to the web version of this article.)

the flow recirculation region between the pin-fins arrays; in all cases, the bubbles are initialised at the edge between the cylinder surface and the base wall of the evaporator. The locations of the nucleation spots tested are shown in Fig. 10, together with snapshots of the bubble dynamics and temperature fields. The images provide a top view of the geometry, where the top wall has been removed to aid visualisation. These snapshots capture the growth of the bubble and the evolution of the temperature field of the heater ($z = 0$), taken at the same time instants for the various nucleation sites tested. When the bubble is initially positioned in the stagnation regions, $\theta = 0, 180°$, there is a more substantial bubble growth. This can be attributed to the bubble being trapped within the static flow region where the fluid is warmer, allowing for an extended period of contact with the walls and, consequently, a more significant growth. The bubble continues to expand symmetrically around the downstream cylinder, and eventually a portion of it escapes from the stagnant region. The high shear exerted by the fluid flowing through the evaporator channels breaks up the bubble into smaller units, which occupy all the channels available and grow until they become elongated bubbles. On the other hand, when the bubble is initialised in a point exposed to the flow outside the stagnant regions, $\theta = 90°$, it detaches quickly from the pin-fin surface due to shear, and thus it grows more slowly. The bubble dynamics observed in Fig. 10 for $\theta = 90°$ resemble those for $\theta = 135°$, where break-up does not occur, and a single elongated bubble unit flows through the channel. It is interesting to note that, although the flow rate is the same for all cases, the elongated bubbles present different shapes depending on the initial position of the nucleation spot. When $\theta = 0$ and 180° multiple bubbles flow through adjacent channels, they do not seem able to expand in the cross-stream gap between the cylinders, while they do so in the cases where $\theta = 90°, 135°$ and only one bubble is present. This is due to the fact that when multiple bubbles are present in adjacent channels, the bubbles cannot displace the liquid out of the recirculation regions as they flow downstream the channel.

Plots of the bubble volume versus time and resulting temperature and heat transfer coefficients are displayed in Fig. 11. As expected, the bubble growth rates are higher when initialised in the stagnation regions. In contrast, the case with $\theta = 90°$ exhibits the slowest growth rate because the bubble departs early from the nucleation spot. Fig. 11(b) and (c) report the spatially-averaged temperatures and heat transfer coefficients for the whole heated surfaces (pin-fins and base wall) as a function of time. For reference, the figure also shows the temporal evolution of temperature and heat transfer coefficient that would be achieved in single-phase, in the absence of nucleation. The heat transfer performance is closely related to the bubble growth rate. When the bubbles grow substantially in the recirculation regions and break up, eventually distributing evenly among the parallel channels, the heat transfer coefficient grows quickly because a larger portion of the heated area is covered by the two-phase flow, and thus, it benefits from more efficient heat transfer mechanisms. The heat transfer coefficient achieved at the end of the simulation for bubbles nucleating at 0 and 180° is about 15% higher than that obtained for bubbles nucleating at 90° or 135°. The beneficial effect of two-phase cooling over single-phase cooling becomes evident at the later time instants, for $t > 0.6\,\mathrm{ms}$, when the bubbles have grown sufficiently large to cover larger areas of the heated surface. As the two-phase flow develops, temperatures drop significantly, and the heat transfer coefficient increases steeply over time, while heat transfer performances deteriorate in single-phase flow as velocity and temperature fields develop towards the steady-state regime.

5.5. Effect of inlet subcooling

In this section, we investigate the impact of the inlet subcooling on the two-phase flow and heat transfer. It is common to have subcooled conditions at the entrance of two-phase heat sinks to prevent boiling onset at the inlet of the evaporator. This may cause backflow of vapour bubbles into the inlet manifold, triggering flow instabilities and maldistribution. Falsetti et al. [18] set the inlet subcooling to $5 \pm 1.5\,\mathrm{K}$ by adjusting the fluid temperature at the inlet manifold plenum of the evaporator using a pre-heater. Using numerical simulations, we study values of inlet subcooling up to $\Delta T_{sub} = 5\,\mathrm{K}$, while keeping mass flux and heat flux constant to $G = 1000\,\mathrm{kg/(m^2 s)}$ and $q = 200\,\mathrm{kW/m^2}$. In this case, a wider domain ($W = 450\,\mu\mathrm{m}$) with three arrays of pin-fins is utilised, and bubbles are nucleated on the central array. Due to subcooling, the location of boiling onset changes along the evaporator depending on ΔT_{sub}, e.g. boiling onset is expected to shift downstream for increasing values of ΔT_{sub}. The procedure adopted to identify the nucleation location for each ΔT_{sub} is explained below.

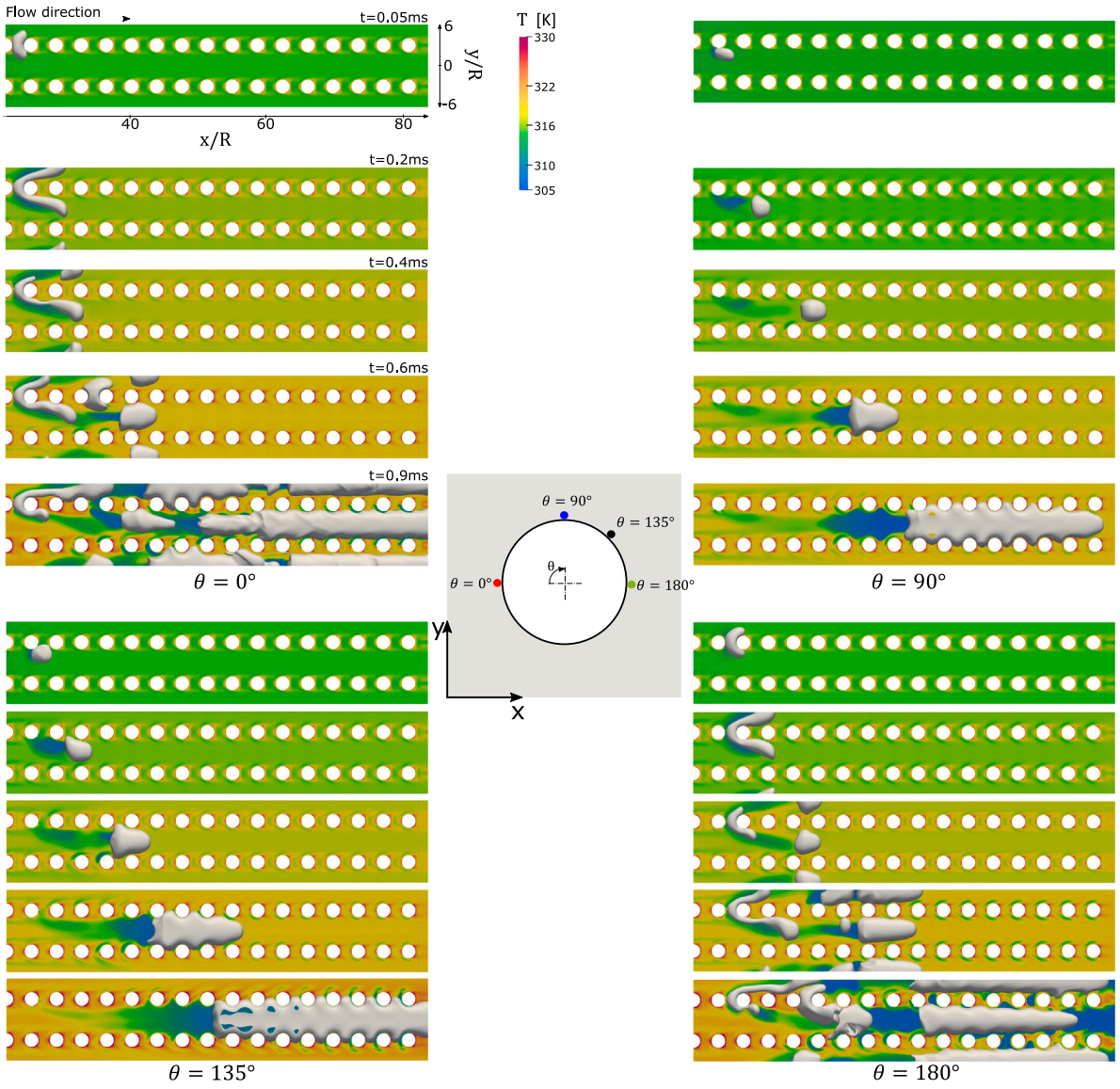

Fig. 10. Systematic analysis of the effect of the location of the nucleation site. Each set of five figures shows snapshots of the bubble profile and temperature field of the base wall ($z = 0$) as time elapses, extracted at the same time instants, for the four different locations of the nucleation site studied. The circumferential position of the nucleation spot around the cylinder is identified by its angle θ calculated as indicated in the inset at the centre of the figure. The results refer to a case run with inlet restrictions, $G = 1000\,\mathrm{kg/(m^2 s)}$, $q = 200\,\mathrm{kW/m^2}$, $T_{sat} = 30\,^{\circ}\mathrm{C}$ and no inlet subcooling.

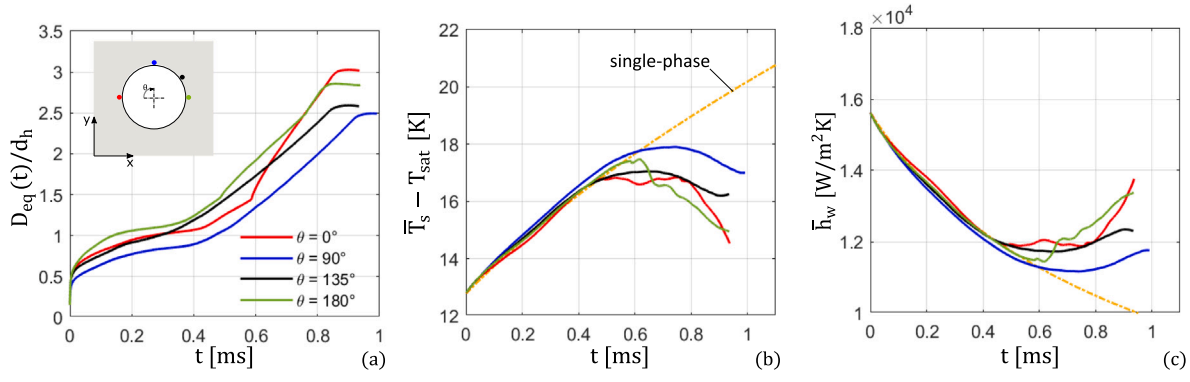

Fig. 11. Systematic analysis of the effect of the location of the nucleation site. (a) Dimensionless bubble equivalent diameter (D_{eq}/d_h) versus time. (b–c) Spatially-averaged temperature ($\overline{T}_s$) and heat transfer coefficient ($\overline{h}_w$) of the heated surfaces (heater and pins) as time elapses. The legend in (a) applies also to (b–c). The results refer to a case run with inlet restrictions, $G = 1000\,\mathrm{kg/(m^2 s)}$, $q = 200\,\mathrm{kW/m^2}$, $T_{sat} = 30\,^{\circ}\mathrm{C}$ and no inlet subcooling.

Table 3
Simulation parameters for the analysis of the effect of subcooling. ΔT_{sub} denotes the inlet subcooling; $\Delta p_{inl-act}$ indicates the single-phase pressure drop between the inlet and the nucleation point, which is located at x_{act}; T_{sat} is the saturation temperature at the nucleation point.

ΔT_{sub} [K]	$T_{sat,inl}$ [K]	T_{inl} [K]	$\Delta p_{inl-act}$ [kPa]	T_{sat} [K]	x_{act} [m]
2	305.95	303.95	1.1	305.8	8.375×10^{-4}
4	305.95	301.95	2.1	305.55	16.75×10^{-4}
5	305.95	300.95	2.5	305.5	20.94×10^{-4}

As a subcooled liquid enters the heat sink, the fluid temperature increases along the flow direction while its pressure and associated saturation temperature decrease due to pressure drop. When the fluid temperature increases above its saturation temperature, boiling is assumed to begin and we define as x_{act} the axial location where this occurs. The pressure and temperature at the inlet of the evaporator were not measured by Falsetti et al. [18], and thus these need to be estimated. In the experiment, the outlet saturation temperature of the fluid was maintained at $T_{sat} = 30.5\,°C$ ($\pm 0.5\,°C$), to which it corresponds a saturation pressure of about $p_{sat} = 325\,kPa$. The total pressure drop in the evaporator measured between inlet and outlet manifold plenums for $G = 1000\,kg/(m^2s)$ and $q = 200\,kW/m^2$ in the experiment in flow boiling conditions was of about 25 kPa. This can be used to estimate the inlet pressure giving $p_{sat,inl} = 350\,kPa$, which corresponds to a saturation temperature of about $T_{sat,inl} = 32.8\,°C$. This is the value considered as the inlet saturation temperature in the present simulations. We study three values of the inlet subcooling, $\Delta T_{sub} = 2\,K, 4\,K, 5\,K$, by setting the inlet temperature in the simulations to $T_{inl} = 30.8\,°C,\ 28.8\,°C,\ 27.8\,°C$. Fig. 12(a) shows the axial profiles of the bulk fluid temperature obtained in single-phase for these three values of ΔT_{sub}. To find the locations of the nucleation sites for each ΔT_{sub}, it is necessary to cross each profile with the profile of the saturation temperature along the evaporator. This is obtained from the single-phase pressure drop in the simulation, giving the red dashed curve in Fig. 12(a). The three nucleation site locations highlighted with blue points in Fig. 12(a) correspond to the x_{act} locations used in the simulations. Table 3 summarises the coordinates of the nucleation spots and corresponding saturation temperatures.

Hence, three different simulations were performed with three different values of inlet subcooling by initialising the vapour bubble at different axial locations along the channel. The bubbles are always initialised on the surface of the nearest pin-fin to the location identified in Table 3, and placed at the edge between the pin-fin surface and bottom wall of the evaporator, at an angle of 135° with the leading edge of the cylinder. An initial single-phase simulation is run for all cases to obtain partially developed velocity and temperature fields. The single-phase simulation terminates when the temperature at the nucleation spot reaches a superheat of 16 K, calculated from the experimental heat transfer coefficient value of $12.5\,kW/(m^2K)$ as explained in Section 4. All simulations were run with a domain length of 3.2 mm.

Fig. 12(b) illustrates the evolution of the dimensionless bubble equivalent diameter over time. Initially, the growths of the bubbles appear to be similar among different subcooling degrees. However, once the bubbles depart from the pin-fin walls, different behaviours emerge. Snapshots of the bubble dynamics at different time instants are displayed in Fig. 12(c) and (d) for $\Delta T_{sub} = 2\,K$ and 4 K, respectively. Upon detachment from the pin-fin walls, the bubbles tend to move towards the centre of the channel, outside the thermal boundary layer. This motion brings them into a region where the surrounding fluid is highly subcooled, particularly near the top surface of the evaporator. Condensation occurs in these regions of the bubble surface and its intensity becomes more significant with higher degrees of subcooling. Every time the bubble approaches a new set of warm pins propelled by the fluid flow, an increase in size is observed, with evaporation becoming dominant over condensation. On the other hand, when the bubble moves away from the set of pins, the surrounding fluid temperature is lower, and the growth of the bubble is arrested until a new set of pins is encountered. This induces oscillations on the plots of the bubble volume over time during the initial stages as manifested by the curves in Fig. 12(b). This oscillatory behaviour becomes more evident as the degree of subcooling increases. For example, in the case of $\Delta T_{sub} = 4\,K$, this oscillatory phase occurs for a longer duration. A subcooling degree of 4 K requires nearly double the time compared to the case with a subcooling of 2 K for this oscillatory stage to terminate. This pattern continues until the bubble reaches a length of approximately $L_b \approx 2R$, which is the minimum size that ensures that the bubble always remains in close contact with the pin-fins. Note that for the highest degree of subcooling studied, $\Delta T_{sub} = 5\,K$, condensation overcomes evaporation, and the bubble condenses completely after departing from the pin-fin surface. For $\Delta T_{sub} = 2\,K$ and 4 K, the development of the bubble shape as it travels through the channel follows a similar pattern to that observed in the previous sections at saturation conditions. The bubble primarily grows in the direction of the flow, driven by the heat transfer from the heater and pin-fins. Once the bubble becomes large enough to fill the square channel cross-section between the cylinders, it expands into the gaps between them. This expansion can be visualised particularly at the time instant e for the test case with a subcooling of $\Delta T_{sub} = 2\,K$, see Fig. 12(c), where an additional effect becomes apparent. Due to the low subcooling and thus high evaporation rate, the bubble begins creating vapour branches penetrating the neighbouring channels. The fluid flow in the empty channels is considerably stronger because the presence of the bubble restricts the free flow of fluid within the channel. Consequently, these vapour branches are pushed and elongated in the direction of the flow. For both $\Delta T_{sub} = 2\,K$ and 4 K, as the bubble approaches the outlet section, dry patches start to form on the surface of the bubble. These are identified as white regions within the bubble in Fig. 12(c) and (d). In the case of a subcooling of 2 K, the area covered by these dry patches is significantly larger, as expected, leading to a decrease in heat transfer performance. Increasing the degree of subcooling results in a reduction in bubble nose velocity and, consequently, in the length of the bubble.

Figs. 13 and 14 present snapshots of the liquid–vapour interface profiles and temperature contours at selected times and over selected planes, together with plots of temperature and heat transfer performances for the cases run with $\Delta T_{sub} = 2\,K$ and $\Delta T_{sub} = 4\,K$. Each figure includes the liquid–vapour interface profiles and temperature contours on the vertical mid-plane $y = 0$ and on two cross-sectional planes orthogonal to the flow direction, for two different time instants, similarly to those previously shown in Fig. 6 for the case with no inlet subcooling. The cylinders near which the $y-z$ cross-sectional planes are extracted are highlighted in green in Fig. 12(c,d). For $\Delta T_{sub} = 2\,K$, Fig. 13(a,b) reveals that at time instant c, the bubble is already slightly elongated, although thick liquid films are still present around the pin-fins surfaces, the top and the bottom walls of the evaporator. Fig. 13(e,f) depict the axial profiles of the average temperature and heat transfer coefficient for each pin-fin at different time instants, and a slight dip in temperature appears at $x/R \approx 50$ at time c, owing to the presence of the bubble. At time e, Fig. 13(c,d), the bubble has expanded in the cross-stream direction with vapour branches extending in the neighbouring channels. Being now confined by the pin-fins and the top/bottom surfaces of the evaporator, the cross-sectional shape of the liquid–vapour interface takes a square or rectangular shape with thin liquid films covering all surfaces. The temperature field on the vertical mid-plane $y = 0$ reveals that the vapour region near the bubble tail has become superheated; this is due to the vapour contact with the heated surface of the evaporator established at the bubble tail, owing to the dryout of the liquid film that was apparent in Fig. 12(c) for $x/R = 70 - 80$. The axial profile of the heat transfer coefficient at time e reported in Fig. 13(f) shows a two-fold increase in the zone occupied by the bubble, reaching peak values of $\overline{h}_{pin} = 25\,kW/(m^2K)$

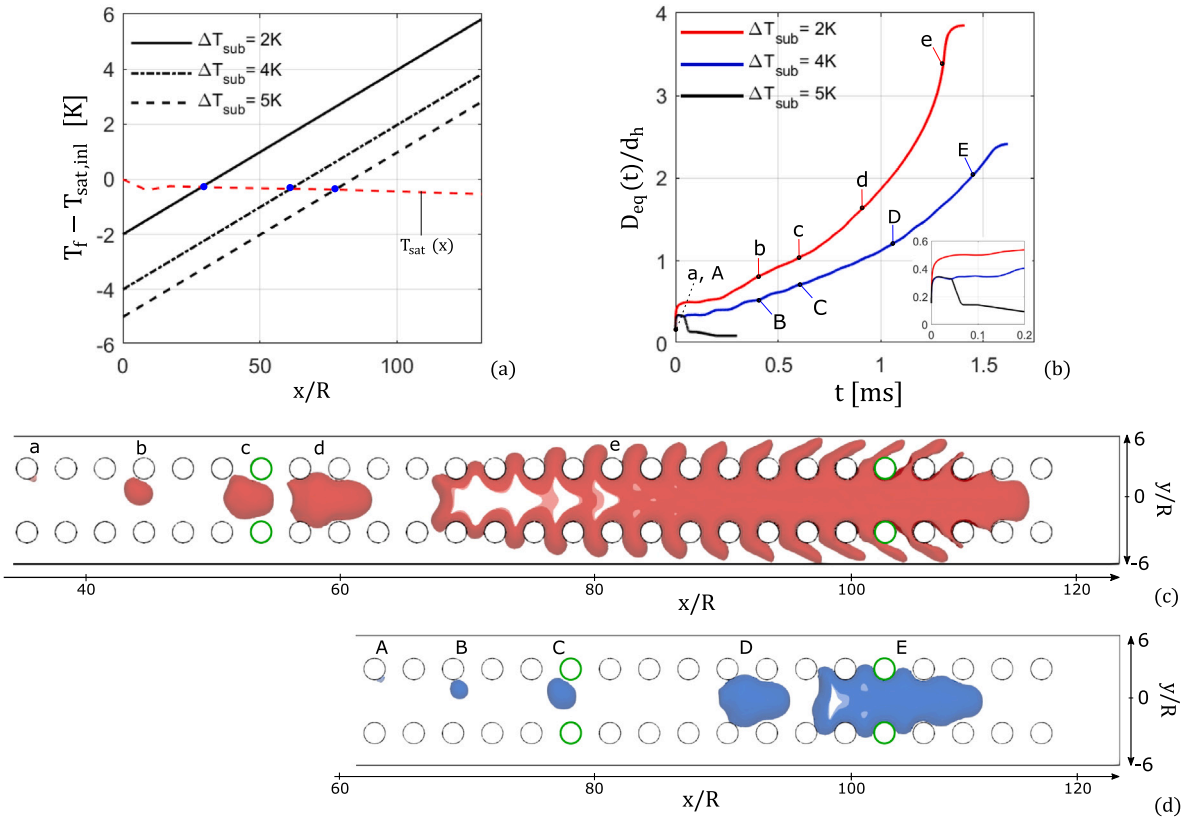

Fig. 12. Systematic analysis of the effect of the subcooling of the fluid at the inlet. (a) Evolution of the bulk temperature (T_f) and locations of the nucleation spots (x_{act}) as a function of the subcooling degree at the inlet. (b) Dimensionless bubble equivalent diameter versus time. The inset shows a close-up view of the first instants of the simulations until the detachment of the bubble occurs. (c) Top view of the bubble profile extracted at the different instants indicated in (b), for subcooling at the inlet $\Delta T_{sub} = 2$ K. (d) Top view of the bubble profile extracted at different instants indicated in (b), for subcooling at the inlet $\Delta T_{sub} = 4$ K. The green cylinders in (c) and (d) identify the cross-sections analysed in Figs. 13 and 14. Other conditions are: $G = 1000\,\mathrm{kg/(m^2 s)}$ and $q = 200\,\mathrm{kW/m^2}$. (For interpretation of the references to colour in this figure legend, the reader is referred to the web version of this article.)

for $x/R = 80-115$, whereas slightly lower values are detected near the bubble tail due to liquid film dryout occurring around the pin-fins.

The situation differs when a higher degree of subcooling, $\Delta T_{sub} = 4$ K, is considered. A comparison of the bubble sizes in Fig. 12(c) and (d) for time instants b ($\Delta T_{sub} = 2$ K) and B ($\Delta T_{sub} = 4$ K), both at $t = 0.4$ ms after nucleation, demonstrates that the bubble diameter at the departure from the nucleation site becomes smaller as subcooling increases. Inspection of the liquid–vapour interface profiles in Fig. 14 indicates that at time instant C ($t = 0.6$ ms, coincident with time c for $\Delta T_{sub} = 2$ K), the bubble is still smaller than the channel size. Thus, its presence is barely perceptible from the temperature and heat transfer coefficients plots in Fig. 14(e) and (f). At time instant E, shortly before reaching the end of the simulation domain, the bubble has become elongated so that very thin liquid films are established around the pin-fins and on the top and bottom evaporator walls, with Fig. 12(d) indicating that film dryout is initiating near the bubble tail. Temperature and heat transfer coefficient at time E exhibit a rapid change from $x/R = 90$, despite the tip of the bubble tail being located at $x/R = 95$. This is because the bubble transit cooled down the wall and reduced the thickness of the thermal boundary layer over the pin-fins and bottom surface of the evaporator, as it is visible in Fig. 14(c), increasing the heat transfer. A peak on the heat transfer coefficient of $\overline{h}_{pin} = 17.5\,\mathrm{kW/(m^2 K)}$ at $x/R \approx 104-108$ is apparent, which corresponds to the two most downstream pin-fins that are fully covered by a thin evaporating film. Since with $\Delta T_{sub} = 4$ K the bubble is shorter, and the pin-fin surface area covered by the evaporating film is smaller than that achieved for $\Delta T_{sub} = 2$ K, the maximum value of the two-phase heat transfer coefficient calculated at instant E is about 30% lower. However, the time-average value calculated over the entire two-phase simulation (red squares in Figs. 13(f) and 14(f)) is slightly higher due to the larger subcooling.

In summary, the results discussed above suggest that a higher degree of subcooling tends to decrease the two-phase heat transfer coefficient because bubbles grow more slowly, thus delaying the beneficial effects of two-phase heat transfer, in agreement with the experimental observations of Chang et al. [21].

6. Conclusions

This article presented the results of a computational study of flow boiling in a micro-pin-fin evaporator. The numerical model of the evaporator included in-line arrays of pin-fins of diameter of 50 μm and height of 100 μm, streamwise pitch of 91.7 μm and cross-stream pitch of 150 μm, to reproduce the micro-pin-fin evaporator studied experimentally by Falsetti et al. [18]. The fluid utilised is refrigerant R236fa at a saturation temperature of 30 °C. The range of operating conditions simulated covers values of mass flux $G = 500-2000\,\mathrm{kg/(m^2 s)}$, heat flux $q = 200\,\mathrm{kW/m^2}$, and inlet subcooling of $\Delta T_{sub} = 0-5$ K. The numerical simulations were performed using a customised version of ESI OpenFOAM v2106, with the built-in geometric Volume Of Fluid method adopted to capture the interface dynamics. The dynamics of the bubbles and thin evaporating liquid films as they evolve through the pin-fin arrays and the corresponding heat transfer mechanisms were studied in detail. The main conclusions of this work are as follows:

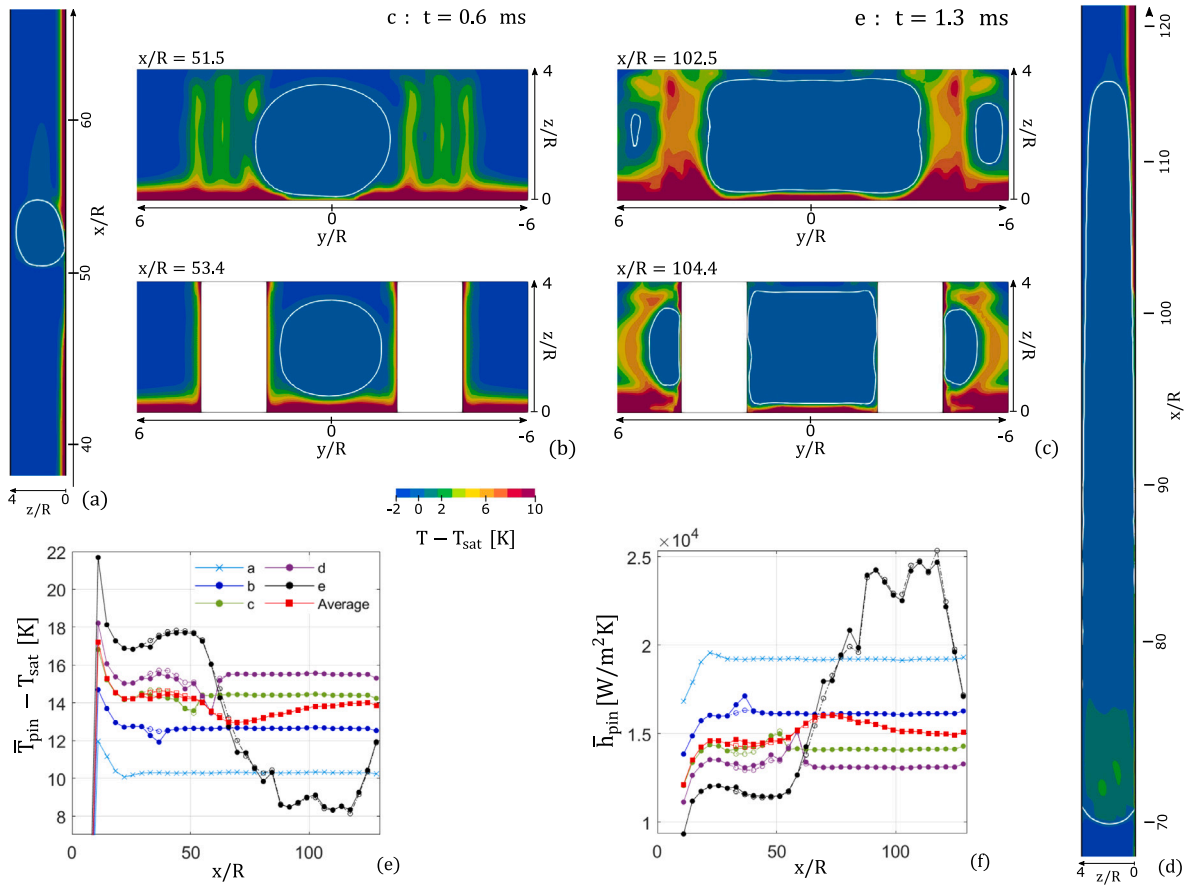

Fig. 13. Simulation results for the case run with an inlet subcooling of $\Delta T_{sub} = 2\,\mathrm{K}$. (a) Liquid–vapour interface profiles and temperature contours on the vertical mid-plane $y = 0$, extracted at time instant c. (b) Liquid–vapour interface profiles and temperature contours on the cross-section at planes $x/R \approx 51$ and 53, extracted at time instant c. (c,d) Liquid–vapour interface profiles and temperature contours on the vertical mid-plane $y = 0$ and cross-sections on planes $x/R \approx 102$ and 104, extracted at time instant e. (e,f) Instantaneous two-phase spatially-averaged temperature ($\overline{T}_{pin}$) and heat transfer coefficient ($\overline{h}_{pin}$) of the pin-fins over the streamwise direction, taken at the time instants indicated in Fig. 12(b). The full markers indicate the results of the array of pin-fins on the side of positive y, where the bubble nucleates, while the empty markers refer to the array of pin-fins on the opposite side ($y < 0$). The graph also shows the time-average results over the entire two-phase simulation. The legend in (e) applies also to (f). The results refer to a case run with inlet restrictions, $G = 1000\,\mathrm{kg/(m^2 s)}$ and $q = 200\,\mathrm{kW/m^2}$.

- In single-phase flow, the flow past the arrays of pin-fins becomes weakly unsteady when the Reynolds number, calculated as $\mathrm{Re} = Gd_h/\mu_l$ with d_h being the hydraulic diameter of the straight channel formed between the arrays, grows above about 400, with vortex shedding visible when $\mathrm{Re} > 600$. While the single-phase friction factor decreases when increasing Re up to $\mathrm{Re} \approx 400$, it exhibits an approximately constant value when Re is above 400 due to the additional pressure drop induced by vortex shedding.
- In single-phase flow, the cylinders exhibit hot spots at circumferential locations identified at 135° from the upstream stagnation point. These hot spots may act as potential nucleation sites, in agreement with existing experimental evidence [20].
- Vapour bubbles nucleated at 135° from the upstream stagnation point detach early from the pin-fin surface and, when no inlet subcooling is set, quickly elongate along the channel formed between the pin-fin arrays. Thin liquid films form around the cylinders, and heat transfer is enhanced by a combination of film evaporation and heat convection in the gaps between the cylinders, with up to +50% increase in Nusselt number compared to the single-phase case for $G = 1000\,\mathrm{kg/(m^2 s)}$.
- Higher flow rates yield higher heat transfer coefficients in the single-phase flow regions of the evaporator, but lower heat transfer coefficients in the two-phase flow region, because the thinner thermal boundary layers reduce the evaporation rates. When G is increased to $2000\,\mathrm{kg/(m^2 s)}$, the overall effect is a reduction in the average heat transfer performance of the evaporator.
- The location of the nucleation site influences the subsequent bubble dynamics and heat transfer significantly. When the bubble nucleates in the stagnation region between consecutive pin-fins (angles of 0° and 180° from the upstream stagnation point), it grows faster and eventually fragments into smaller bubbles. This increases the surface area covered by the two-phase flow and leads to an average heat transfer coefficient that is about 16% higher than that observed for bubbles nucleating at 90°.
- Higher inlet subcooling decreases the two-phase heat transfer coefficients due to condensation occurring when bubbles depart from the hot pin-fin surfaces. At a subcooling of 5 K, bubbles collapse completely once they depart from the pin-fins.

In conclusion, the dynamics of bubbles and flow boiling in micro-pin-fin evaporators are significantly different from those observed in straight microchannels. Computational heat transfer prediction models would benefit from the availability of finely resolved experimental data for film thickness, bubble dynamics and local heat transfer measurements, which are becoming increasingly available for straight channels but are not yet available for two-phase flows across pin-fin geometries.

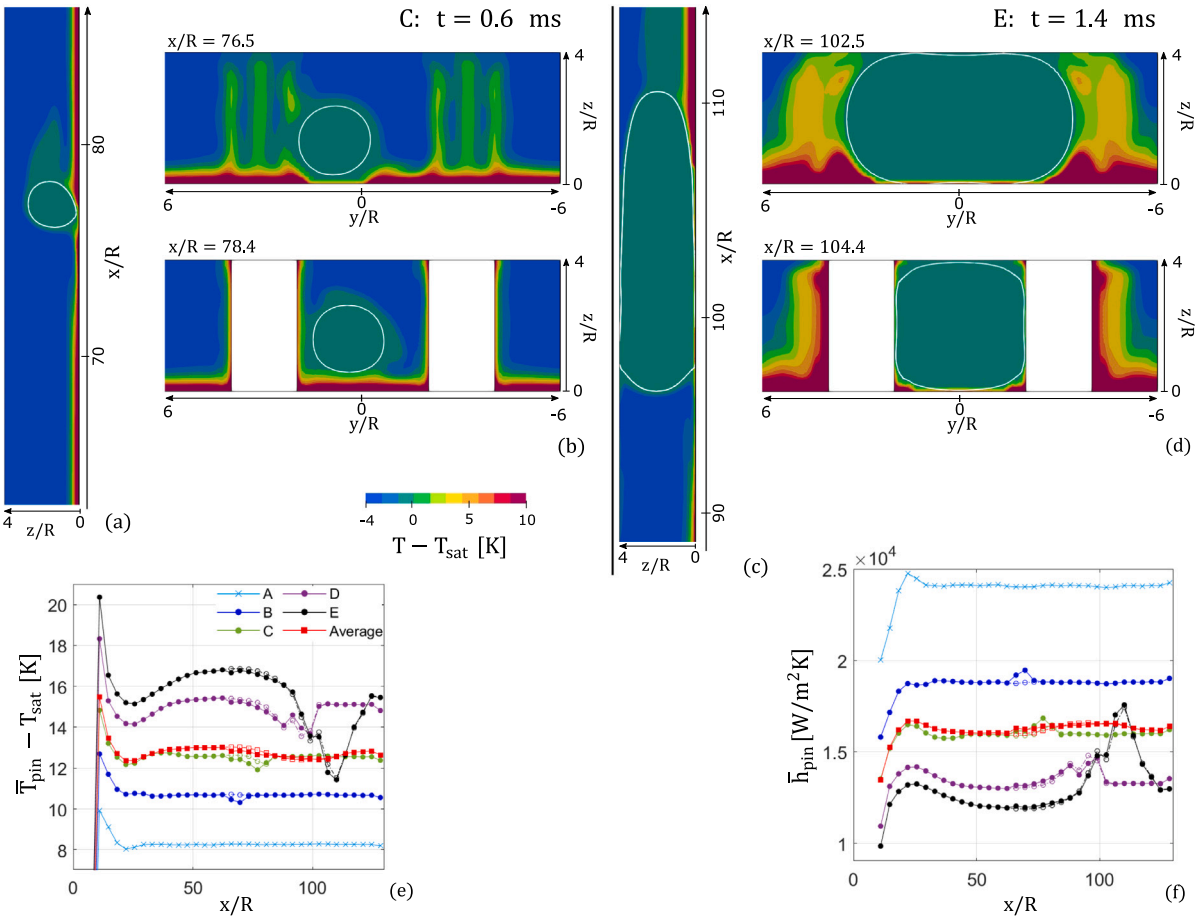

Fig. 14. Simulation results for the case run with an inlet subcooling of $\Delta T_{sub} = 4\,\mathrm{K}$. (a) Liquid–vapour interface profiles and temperature contours on the vertical mid-plane $y = 0$, extracted at time instant C. (b) Liquid–vapour interface profiles and temperature contours on the cross-section at planes $x/R \approx 76$ and 78, extracted at time instant C. (c,d) Liquid–vapour interface profiles and temperature contours on the vertical mid-plane $y = 0$ and cross-sections on planes $x/R \approx 102$ and 104, extracted at time instant E. (e,f) Instantaneous two-phase spatially-averaged temperature ($\overline{T}_{pin}$) and heat transfer coefficient ($\overline{h}_{pin}$) of the pin-fins over the streamwise direction, taken at the time instants indicated in Fig. 12(b). The full markers indicate the results of the array of pin-fins on the side of positive y, where the bubble nucleates, while the empty markers refer to the array of pin-fins on the opposite side ($y < 0$). The graph also shows the time-average results over the entire two-phase simulation. The legend in (e) applies also to (f). The results refer to a case run with inlet restrictions, $G = 1000\,\mathrm{kg/(m^2 s)}$ and $q = 200\,\mathrm{kW/m^2}$.

CRediT authorship contribution statement

I. El Mellas: Conceptualization, Methodology, Software, Validation, Visualization, Writing – original draft, Writing – review & editing. **N. Samkhaniani:** Software, Validation, Writing – review & editing. **C. Falsetti:** Conceptualization, Validation, Writing – review & editing. **A. Stroh:** Funding acquisition, Supervision, Writing – review & editing. **M. Icardi:** Supervision, Writing – review & editing. **M. Magnini:** Conceptualization, Data curation, Funding acquisition, Methodology, Project administration, Resources, Supervision, Visualization, Writing – original draft, Writing – review & editing.

Declaration of competing interest

The authors declare that they have no known competing financial interests or personal relationships that could have appeared to influence the work reported in this paper.

Data availability

Data will be made available on request.

Acknowledgements

M. Magnini acknowledges the support of the UK Engineering & Physical Sciences Research Council (grant EP/T033398/1). Calculations were performed using Sulis Tier-2 HPC platform hosted by the Scientific Computing Research Technology Platform at the University of Warwick. Sulis is funded by EPSRC, United Kingdom Grant EP/T022108/1 and the HPC Midlands+ consortium. N. Samkhaniani and A. Stroh acknowledge the support by the German Research Foundation (DFG) through the Research Unit 2383 ProMiSe under Grant No. STR 1585/2-1.

References

[1] T.G. Karayiannis, M.M. Mahmoud, Flow boiling in microchannels: Fundamentals and applications, Appl. Therm. Eng. 115 (2017) 1372–1397.
[2] D. Tuckerman, R. Pease, High-performance heat sinking for VLSI, Electron Device Lett. 2 (1981) 126–129.
[3] C. Baldassari, M. Marengo, Flow boiling in microchannels and microgravity, Prog. Energy Combust. Sci. 39 (2013) 1–36.
[4] M. Asadi, G. Xie, B. Sunden, A review of heat transfer and pressure drop characteristics of single and two-phase microchannels, Int. J. Heat Mass Transfer 79 (2014) 34–53.

[5] L. Cheng, G. Xia, Fundamental issues, mechanisms and models of flow boiling heat transfer in microscale channels, Int. J. Heat Mass Transfer 108 (2017) 97–127.
[6] Y. Peles, A. Kosar, C. Mishra, C. Kuo, B. Schneider, Forced convective heat transfer across a pin fin micro heat sink, Int. J. Heat Mass Transfer 48 (2005) 3615–3627.
[7] A. Mohammadi, A. Kosar, Review on heat and fluid flow in micro pin fin heat sinks undersingle-phase and two-phase flow conditions, Nanoscale Microscale Thermophys. Eng. 22 (2018) 153–197.
[8] D. Deng, L. Zeng, W. Sun, A review on flow boiling enhancement and fabrication of enhanced microchannels of microchannel heat sinks, Int. J. Heat Mass Transfer 175 (2021) 121332.
[9] J.F. Tullius, R. Vajtai, Y. Bayazitoglu, A review of cooling in microchannels, Heat Transf. Eng. 32 (2011) 527–541.
[10] R. Ricci, S. Montelpare, An experimental IR thermographic method for the evaluation of the heat transfer coefficient of liquid-cooled short pin fins arranged in line, Exp. Therm. Fluid Sci. 30 (2006) 381–391.
[11] W. Wan, D. Deng, Q. Huang, T. Zeng, Y. Huang, Experimental study and optimization of pin fin shapes in flow boiling of micro pin fin heat sinks, Appl. Therm. Eng. 114 (2017) 436–449.
[12] R. Sun, J. Hua, X. Zhang, X. Zhao, Experimental study on the effect of shape on the boiling flow and heat transfer characteristics of different pin-fin microchannels, Int. J. Heat Mass Transfer 57 (2021) 2081–2095.
[13] X. Yu, C. Woodcock, Y. Wang, J. Plawsky, Y. Peles, Enhanced subcooled flow boiling heat transfer in microchannel with piranha pin fin, Int. J. Heat Mass Transfer 139 (2017) 112402.
[14] A. Kosar, Y. Peles, Convective flow of refrigerant (R-123) across a bank of micro pin fins, Int. J. Heat Mass Transfer 49 (2006) 3142–3155.
[15] A. Kosar, Y. Peles, Boiling heat transfer in a hydrofoil-based micro pin fin heat sink, Int. J. Heat Mass Transfer 50 (2007) 1018–1034.
[16] S. Krishnamurthy, Y. Peles, Flow boiling of water in a circular staggered micro-pin fin heat sink, J. Heat Transfer 51 (2008) 1349–1364.
[17] M. Law, P. Lee, A comparative study of experimental flow boiling heat transfer and pressure characteristics in straight- and oblique-finned microchannels, Int. J. Heat Mass Transfer 85 (2014) 797–810.
[18] C. Falsetti, H. Jafarpoorchekab, M. Magnini, N. Borhani, J.R. Thome, Two-phase operational maps, pressure drop, and heat transfer for flow boiling of R236fa in a micro-pin fin evaporator, Int. J. Heat Mass Transfer 107 (2017) 805–819.
[19] C. Falsetti, M. Magnini, J.R. Thome, Flow boiling heat transfer and pressure drops of R1234ze(E) in a silicon micro-pin fin evaporator, J. Electron. Packag. 139 (2017) 031008.
[20] C. Falsetti, M. Magnini, J.R. Thome, Hydrodynamic and thermal analysis of a micro-pin fin evaporator for on-chip two-phase cooling of high density power micro-electronics, Appl. Therm. Eng. 130 (2018) 1425–1439.
[21] W.R. Chang, C.A. Chen, J.H. Ke, T.F. Lin, Subcooled flow boiling heat transfer and associated bubble characteristics of FC-72 on a heated micro-pin-finned silicon chip, Int. J. Heat Mass Transfer 53 (2009) 5605–5621.
[22] M. Magnini, B. Pulvirenti, J.R. Thome, Numerical investigation of hydrodynamics and heat transfer of elongated bubbles during flow boiling in a microchannel, Int. J. Heat Mass Transfer 59 (2013) 451–471.
[23] M. Magnini, O.K. Matar, Numerical study of the impact of the channel shape on microchannel boiling heat transfer, Int. J. Heat Mass Transfer 150 (2020) 119322.
[24] F. Municchi, I. El Mellas, O.K. Matar, M. Magnini, Conjugate heat transfer effects on flow boiling in microchannels, Int. J. Heat Mass Transfer 195 (2022).
[25] D. Lorenzini, Y. Joshi, Flow boiling heat transfer in silicon microgaps with multiple hotspots and variable pin fin clustering, Phys. Fluids 31 (2019) 102002.
[26] I. El Mellas, F. Municchi, M. Icardi, M. Magnini, Dynamics of long bubbles propagating through cylindrical micro-pin fin arrays, Int. J. Multiph. Flow 163 (2023) 104443.
[27] G. Tryggvason, R. Scardovelli, S. Zaleski, Direct Numerical Simulations of Gas-Liquid Multiphase Flows, Cambridge University Press, Cambridge, 2011.
[28] J. Roenby, H. Bredmose, H. Jasak, A computational method for sharp interface advection, R. Soc. Open Sci. 3 (2016) 160405.
[29] H. Scheufler, J. Roenby, Accurate and efficient surface reconstruction from volume fraction data on general meshes, J. Comput. Phys. 383 (2019) 1–23.
[30] R.W. Schrage, A Theoretical Study of Interphase Mass Transfer, Columbia University Press, New York, 1953.
[31] J.U. Brackbill, D.B. Kothe, C. Zemach, A continuum method for modeling surface tension, J. Comput. Phys. 100 (1992) 335–354.
[32] S. Hardt, F. Wondra, Evaporation model for interfacial flows based on a continuum-field representation of the source terms, J. Comput. Phys. 227 (2008) 5871–5895.
[33] I. Tanasawa, Advances in condensation heat transfer, in: J.P. Hartnett, T.F. Irvine (Eds.), Advances in Heat Transfer, Academic Press, San Diego, 1991.
[34] A. Ferrari, M. Magnini, J.R. Thome, Numerical analysis of slug flow boiling in square microchannels, Int. J. Heat Mass Transfer 123 (2018) 928–944.
[35] B. van Leer, Towards the ultimate conservative difference scheme. V. A second-order sequel to Godunov's method, J. Comput. Phys. 32 (1979) 101–136.
[36] R.I. Issa, Solution of the implicitly discretized fluid flow equations by operator-splitting, J. Comput. Phys. 62 (1985) 40–65.
[37] S. Jones, G. Evans, K. Galvin, Bubble nucleation from gas cavities — a review, Adv. Colloid Interface Sci. 80 (1999) 27–50.
[38] M. Magnini, O.K. Matar, Morphology of long gas bubbles propagating in square capillaries, Int. J. Multiph. Flow 129 (2020) 103353.
[39] M. Magnini, J.R. Thome, Computational study of saturated flow boiling within a microchannel in the slug flow regime, J. Heat Transfer 138 (2016) 021502.
[40] T. Brunschwiler, B. Michel, H.E. Rothuizen, U. Kloter, B. Wunderle, H. Oppermann, H. Reichl, Interlayer cooling potential in vertically integrated packages, Microsyst. Technol. 15 (2008) 57–74.
[41] A. Zukauskas, Some aspects of heat transfer from tubes in crossflow, in: The 1996 4 Th International Symposium on Heat Transfer, ISHT, Beijing, China, 10/07-11/96, 1996, pp. 82–93.
[42] S. Zhang, N. Cagney, S. Balabani, C.P. Naveira-Cotta, M.K. Tiwari, Probing vortex-shedding at high frequencies in flows past confined microfluidic cylinders using high-speed microscale particle image velocimetry, Phys. Fluids 31 (2019) 102001.
[43] P.-S. Lee, S.V. Garimella, Saturated flow boiling heat transfer and pressure drop in silicon microchannel arrays, Int. J. Heat Mass Transfer 51 (2008) 789–806.
[44] V. Gesellschaft, VDI Heat Atlas, Springer Berlin Heidelberg, 2010.
[45] F. Incropera, Fundamentals of Heat and Mass Transfer 6th Edition, John Wiley and Sons, 2011.
[46] C. Falsetti, M. Magnini, J.R. Thome, A new flow pattern-based boiling heat transfer model for micro-pin fin evaporators, Int. J. Heat Mass Transfer 122 (2018) 1425–1439.
[47] S. Khodaparast, M. Magnini, N. Borhani, J.R. Thome, Dynamics of isolated confined air bubbles in liquid flows through circular microchannels: an experimental and numerical study, Microfluid Nanofluidics 19 (2015) 209–234.
[48] M. Magnini, A. Ferrari, J.R. Thome, H.A. Stone, Undulations on the surface of elongated bubbles in confined gas-liquid flows, Phys. Rev. Fluids 2 (2017) 084001.